

# Radiative forcing and vertical heating rate of dust aerosols in southwestern Tajikistan during summer 2023

Zhengpeng Li<sup>a</sup>, Zhongwei Huang<sup>a,b,\*</sup>, Jianrong Bi<sup>a,b,c</sup>, Qingqing Dong<sup>a</sup>, Yongkai Wang<sup>a</sup>, Sabur F. Abdullaev<sup>d</sup>, Dilovar Nozirov<sup>d</sup>, Wuren Li<sup>b</sup>, Ze Li<sup>b</sup>, Zhaozhao Meng<sup>b</sup>, Wentao Liu<sup>b</sup>, Xiaodong Song<sup>b</sup>

<sup>a</sup> Key Laboratory for Semi-Arid Climate Change of the Ministry of Education, College of Atmospheric Sciences, Lanzhou University, Lanzhou, 730000, China

<sup>b</sup> Collaborative Innovation Center for Western Ecological Safety, Lanzhou University, Lanzhou, 730000, China

<sup>c</sup> Gansu Provincial Field Scientific Observation and Research Station of Semi-arid Climate and Environment, Lanzhou, 730000, China

<sup>d</sup> Physical-Technical Institute, Academy of Sciences of Republic of Tajikistan, Dushanbe, 734063, Tajikistan

## HIGHLIGHTS

- The net radiative forcing of dust aerosols at TOA was positive at Shaartuz.
- Heavy dust exhibited a double-layer shortwave heating characteristic.
- The dust longwave heating at the surface compensated for 34–43% of shortwave cooling.

## ARTICLE INFO

### Keywords:

Dust aerosols  
Radiative forcing  
Vertical heating rate

## ABSTRACT

The radiative effects of dust aerosol are essential for understanding the thermal and dynamic structure of the atmosphere, along with the energy balance of the Earth's atmospheric system. This study assessed the radiative forcing and vertical heating rate of dust aerosols at Shaartuz, Tajikistan, during the summer of 2023, utilizing data from the sun sky lunar photometer, lidar, and a radiative transfer model. The results indicated that the daily average shortwave radiative forcings of dust aerosols were  $-32.0 \text{ W m}^{-2}$  at the surface and  $30.5 \text{ W m}^{-2}$  in the atmosphere during heavy dust conditions, which were roughly three times greater than those observed with light dust. The daily averages of longwave radiative heating at the surface compensated for 34.2%, 39.0%, and 43.1% of shortwave cooling under light, moderate, and heavy dust conditions, respectively. The net radiative forcing efficiencies (NRFE) were  $-30.2$ ,  $42.5$ , and  $12.3 \text{ W m}^{-2} \text{ AOD}^{-1}$  at the surface, in the atmosphere, and at the top of the atmosphere (TOA), respectively. The maximum shortwave heating rates (SHR) of dust aerosols below 500 m were 0.7, 1.1, and  $2.1 \text{ K day}^{-1}$  for light, moderate, and heavy dust conditions, respectively. Under conditions of heavy dust presence, the SHR attained  $1.7 \text{ K day}^{-1}$  at an altitude of 3 km, resulting in alterations to the initial thermal configuration of the atmosphere and surface temperature. The maximum surface temperature recorded in heavy dust conditions was  $8.6 \text{ }^{\circ}\text{C}$  ( $5.9 \text{ }^{\circ}\text{C}$ ) lower than the temperatures observed in light dust (moderate dust) conditions. The results contribute to a deeper comprehension of how dust aerosols influence the radiation budget within the Earth's atmospheric system in Central Asia.

## 1. Introduction

Dust aerosols, a primary category of aerosols in the troposphere, can absorb and scatter both shortwave (SW) and longwave (LW) radiation, which constitutes their direct effects. This interaction plays a crucial role

in influencing the radiation balance of the Earth (Huang et al., 2014; Ryder et al., 2019), thereby carrying substantial implications for the energy budget of the Earth's atmospheric system. The direct radiative forcing of dust aerosols has the potential to significantly alter surface temperature (Liu et al., 2021; Saidou Chaibou et al., 2020; Xie et al.,

\* Corresponding author. Key Laboratory for Semi-Arid Climate Change of the Ministry of Education, College of Atmospheric Sciences, Lanzhou University, Lanzhou, 730000, China.

E-mail address: [huangzhongwei@lzu.edu.cn](mailto:huangzhongwei@lzu.edu.cn) (Z. Huang).

<https://doi.org/10.1016/j.atmosenv.2025.121051>

Received 16 October 2024; Received in revised form 5 January 2025; Accepted 17 January 2025

Available online 22 January 2025

1352-2310/© 2025 Elsevier Ltd. All rights are reserved, including those for text and data mining, AI training, and similar technologies.

2018). The impact of dust aerosols on regional temperatures, which is comparable to the temperature changes expected from rising greenhouse gas concentrations over recent decades, underscores the importance of incorporating dust aerosols into climate change research (Zhang et al., 2009). Dust aerosols contribute to atmospheric heating, modify the inherent thermal structure, and consequently influence weather systems (Chen et al., 2023; Pan et al., 2024) as well as regional precipitation patterns (Wang et al., 2022). Chen et al. (2023) demonstrated that the Mongolian cyclone dominated the dust storm in May 2019. The radiation feedback from the dust storm altered the vertical thermal structure of the atmosphere, enhancing baroclinicity. This intensification of the Mongolian cyclone led to the persistence of the strong dust storm. Pan et al. (2024) conducted sensitivity experiments showing that the radiation effect of Sahara dust amplified the mid-level ridge in the central Atlantic through temperature disturbances, thereby altering the path and intensity of two tropical cyclones. Wang et al. (2022) indicated that the radiative forcing of dust aerosols can strengthen the West African summer monsoon by enhancing the ocean-land thermal gradient. However, due to differences in the assumed absorption efficiency of dust aerosols in the models, Wang et al. (2022)'s results contradict those of Miller et al. (2004) and Jordan et al. (2018).

Some scholars constrained the direct radiative effect of dust to a range between  $-0.48$  and  $+0.20 \text{ W m}^{-2}$ , which includes the possibility that dust causes a net cooling or warming of the planet (Kok et al., 2017). The Sixth Assessment Report of the Intergovernmental Panel on Climate Change (IPCC) highlighted that the uneven spatial distribution of aerosol concentration, types, and optical properties, combined with insufficient long-term observational data in certain areas, contributes to the uncertainty in quantifying the radiative effects of aerosols. This uncertainty renders the climate effects of aerosols as one of the most ambiguous elements in climate assessment and prediction (Intergovernmental Panel on ClimateC, 2023). The increase in global dust aerosols since pre-industrial times is estimated at  $55 \pm 30\%$ . This rise has resulted in a global mean effective radiative forcing of  $-0.07 \pm 0.18 \text{ W m}^{-2}$ , which somewhat mitigates the effects of greenhouse warming (Kok et al., 2023). The numerical assessment of the direct radiative impact of dust aerosols across various global regions presents considerable uncertainty. Quijano et al. (2000) found that the magnitudes of the heating rates from Saharan dust can be 25% greater than those from Afghan dust when the sun is at high angles and over bright surfaces. Li et al. (2004) estimated that diurnal mean SW forcing efficiency at the top of the atmosphere (TOA) of Saharan dust is  $-35 \pm 3 \text{ W m}^{-2} \text{ AOD}^{-1}$  for the high-dust months and  $-26 \pm 3 \text{ W m}^{-2} \text{ AOD}^{-1}$  for the low-dust months near the African coast. Several studies have highlighted the significance of LW radiation effects caused by dust aerosols in the Mediterranean region (Kokkalis et al., 2021; Meloni et al., 2015; Sicard et al., 2014; Soupionna et al., 2020). Huang et al. (2009) utilized satellite data along with the Fu Liou model (Fu and Liou, 1992, 1993) to demonstrate that dust aerosols can increase atmospheric temperatures by up to 1, 2, and 3  $\text{K day}^{-1}$  in environments with light, moderate, and heavy dust layers, respectively, over the Taklimakan Desert in July 2006. The daily mean net radiative effect of the dust is  $44.4 \text{ W m}^{-2}$  at the TOA,  $-41.9 \text{ W m}^{-2}$  at the surface, and  $86.3 \text{ W m}^{-2}$  in the atmosphere (Huang et al., 2009).

Currently, research on the radiation effects of dust aerosols predominantly centers on the Sahara Desert, Taklamakan Desert, and their adjacent regions, with little attention paid to Central Asia. This region is situated at the core of the global dust belt, characterized by multiple deserts. Consequently, it frequently experiences the impact of dust aerosols (Hofer et al., 2017) and is landlocked, exhibiting low precipitation levels and high evaporation rates (Lioubimtseva and Henebry, 2009). More than 60% of the area is classified as arid to semi-arid, positioning it among the driest regions globally. This characteristic renders the region particularly sensitive and vulnerable to the effects of rapid climate change (Hu and Han, 2022; Hua et al., 2022). In recent decades, there has been a notable increase in temperatures accompanied

by frequent heat waves (Wang et al., 2023; Yu et al., 2020), and the desert climate has extended northward by over 100 km in Central Asia (Hu and Han, 2022). The role of dust aerosols in the climate change of the region is a topic worth exploring, but due to economic conditions and the natural environment, there are relatively few observations of dust aerosols in the region. Bi et al. (2016) gathered columnar key absorption and optical properties of mineral dust in Central Asian regions by employing multiyear quality-assured datasets collected at Aerosol Robotic Network (AERONET) sites. Li and Sokolik (2018) conducted a simulation of a dust event in Central Asia, highlighting the significance of dust composition and surface albedo in the assessment of dust radiative forcing. Hofer et al. (2017, 2020) employed ground-based lidar in Dushanbe, the capital of Tajikistan, to acquire the vertical optical characteristics of aerosols. Rupakheti et al. (2020, 2021) analyzed the radiative effects of dust aerosols by utilizing AERONET data collected from Dushanbe. Research on dust aerosols in Tajikistan primarily concentrated on the capital, Dushanbe, owing to infrastructural constraints. The systematic observation of dust aerosols in the southwestern region of Tajikistan traced back to the last century (Gillette et al., 1993; Golitsyn and Gillette, 1993; Sokolik and Golitsyn, 1993). This region serves as a significant pathway for the eastward movement of dust aerosols from the west to Dushanbe (Golitsyn and Gillette, 1993). Understanding this process is essential for analyzing the transport and radiative impacts of dust aerosols in Tajikistan and throughout Central Asia.

A precise evaluation of the direct radiative impacts of dust aerosols is essential for comprehending the radiation balance within the Earth's atmospheric system. However, considerable uncertainty remains in the models' estimation of the direct radiation effects of dust aerosols at the regional scale, primarily due to insufficient observational data. In June 2023, the Semi-Arid Climate and Environment Observatory of Lanzhou University (SACOL) collaborated with the Physical-Technical Institute of the Academy of Sciences of the Republic of Tajikistan to establish a super observatory, located at Ayyvaj, Shaartuz, southwest Tajikistan. The super observatory aims to investigate the impact of dust aerosols in this region utilizing instruments such as the sun sky lunar photometer, lidar, environmental dust monitor, and automatic meteorological station. This study utilized data collected at Shaartuz during the summer months (June to August) of 2023, in conjunction with a radiative transfer model, to simulate the direct radiative forcing and heating rate of dust aerosols. It aims to quantitatively assess the influence of dust aerosols on the radiative budget for the summer season. The structure of the article is outlined as follows. Section 2 presents a concise summary of the site and the instruments used. Section 3 presents a concise overview of the methodology and model employed. Section 4 presents an analysis of the direct radiative forcing and heating rate associated with dust aerosols. Section 5 presents a discussion and summary of the findings from this study.

## 2. Site description and instruments

### 2.1. Site description

Shaartuz is situated on the southwestern border of Tajikistan, neighboring Afghanistan. The population density in this area is low, and the influence of anthropogenic aerosols is relatively small, which provides more favorable conditions for examining the effects of dust aerosols at Shaartuz in comparison to Dushanbe. The site experiences a mean annual temperature of  $17.1 \text{ }^\circ\text{C}$  and a mean annual precipitation of 223 mm, characteristic of a semi-arid climate. The region experiences minimal precipitation, primarily occurring during the winter and spring seasons. Fig. 1 illustrates a vast expanse of barren land and desert located to the west of the site, which experiences ongoing influence from dust aerosols from April through November (Abdullaev et al., 2013; Abdullaev and Sokolik, 2019). The site is both a source and a receptor of dust aerosols, serving as a key pathway for the transport of dust aerosols

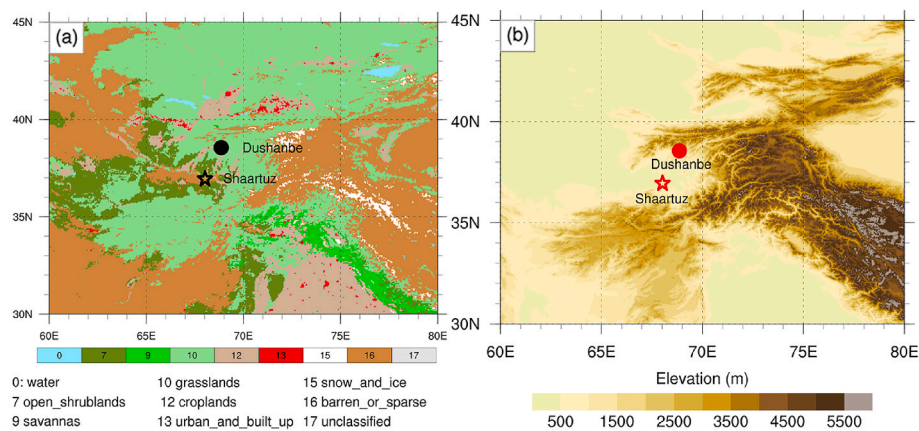


Fig. 1. (a) Land cover types and (b) elevation in Tajikistan and its surrounding areas. The star represents the location of observational site studied in the paper.

to the capital, Dushanbe (Golitsyn and Gillette, 1993), and the Pamir Plateau (Smirnov et al., 1993). The region is surrounded by mountains on three sides, a geographic feature that facilitates the accumulation of dust aerosols, making it an ideal site for studying the transport and impact of Central Asian dust aerosols.

## 2.2. Measuring instruments

Lidar is an effective instrument to detect the vertical structure of aerosols and clouds (Huang et al., 2010, 2023; Siqi et al., 2021; Zhang et al., 2023). To gather detailed information on dust aerosols, we utilized a dual-wavelength polarization Raman lidar at Shaartuz to measure tropospheric aerosol attenuated backscatter coefficients at 532 and 1064 nm, as well as the volume depolarization ratio at 532 nm during both daytime and nighttime (Huang et al., 2018; Liu et al., 2024). The temporal resolution is set at 2 min, while the vertical spatial resolution measures 7.5 m. The blind area of the Raman Lidar is about 180 m. The Cimel sun sky lunar photometer (CE318 T) installed at the site serves as a crucial instrument within the Aerosol Robotic Network (AERONET). It is capable of accurately measuring aerosol optical depth (AOD), Ångström exponent (AE), and water vapor column content (WV) during both daytime and nighttime (Bi et al., 2013, 2024). The Level 1.5 data of CE 318 T have undergone pre- and post-field calibration, along with automatic cloud screening (Barreto et al., 2013; Giles et al., 2019). Previous studies have shown that there is an uncertainty of 0.01–0.02 in AOD (wavelength dependent) and Uncertainty in the water vapor retrieval is typically less than 12% because of calibration uncertainty for the field instruments (Eck et al., 1999; Holben et al., 1998). The Grimm 180 is capable of measuring aerosol particle concentration, allowing us to utilize PM<sub>2.5</sub> (particulate matter with a diameter of less than 2.5 μm) and PM<sub>10</sub> (particulate matter with a diameter of less than 10 μm) data in the article. The automatic meteorological station is equipped with various instruments, including a radiometer (CNR4), infrared temperature sensor (SI-411), barometer (CS106), humidity and temperature probe (HMP155A), wind sensor (WindSonic), rain gage (TE525MM), and soil sensor (CS655). It is capable of measuring a range of parameters, such as surface radiative flux, surface albedo, surface temperature, air pressure, humidity, wind speed, precipitation, soil temperature, and soil moisture.

## 2.3. Auxiliary data

The Moderate Resolution Imaging Spectroradiometer (MODIS) sensors, which function on the Terra (around 10:30 a.m. local time) and Aqua (around 1:30 p.m. local time) satellites, have been widely utilized in numerous studies (Justice et al., 2002). The article utilizes the most recent version of “MODIS Land Cover Type Yearly.” The Ozone

Monitoring Instrument (OMI) functions as an ultraviolet/visible nadir solar backscatter spectrometer, delivering almost complete global coverage of ozone (Kanniah et al., 2020; Levelt et al., 2018).

The analysis employed the new-generation reanalysis data from the European Center for Medium-Range Weather Forecasts (ERA5) and the Modern Era Retrospective Analysis for Research and Applications, version 2 (MERRA2). The reanalysis data incorporate various sources of information, including conventional observations from surface weather stations, balloons, aircraft, ships, buoys, and satellites (Gelaro et al., 2017; Hersbach et al., 2020).

## 3. Methodology

### 3.1. Retrieval of lidar profile

The lidar’s raw signals underwent pre-processing, which included background correction, range correction, polarization correction, and overlap correction, before further analysis (Huang et al., 2020; Wang et al., 2018). The attenuated backscatter coefficient (ABC) and the volume depolarization ratio (VDR) are defined as follows (Zhang et al., 2022),

$$ABC_{\lambda,r} = \frac{P_{\perp,\lambda,r} + P_{\parallel,\lambda,r}}{K_{\lambda} C_{\lambda} G_{\lambda,r}} \quad (1)$$

$$VDR_{\lambda,r} = \frac{P_{\perp,\lambda,r}}{P_{\parallel,\lambda,r} K_{\lambda}} \quad (2)$$

Where  $P_{\perp,\lambda,r}$  and  $P_{\parallel,\lambda,r}$  represent the horizontal and polarization signals, respectively, at different wavelengths  $\lambda$  in the distance  $r$ .  $K_{\lambda}$ ,  $C_{\lambda}$ ,  $G_{\lambda,r}$  are the lidar polarization calibration ratio, the system lidar constant, and the overlap factor of Raman lidar at wavelength  $\lambda$  in the distance  $r$ .

The aerosol extinction coefficient ( $\sigma_1$ ) was obtained using Fernald’s method (Dong et al., 2022; Fernald, 1984).

$$[A(I-1, I)] = (S_1 - S_2) [\beta_2(I-1) + \beta_2(I)] \Delta Z \quad (3)$$

$$\sigma_1(I-1) = \frac{X(I-1) \exp[A(I-1, I)]}{\frac{X(I)}{\sigma_1(I) + S_2 \sigma_2(I)} + \{X(I) + X(I-1) \exp[A(I-1, I)]\} \Delta Z} - \frac{S_1}{S_2} \sigma_2(I-1) \quad (4)$$

where  $S_1$  (50 sr, Liu et al., 2002) and  $S_2$  ( $8\pi/3$ ) are the lidar ratios of aerosols and air molecules, respectively.  $\beta_2$  represents the backscattering coefficient of air molecules, while  $\Delta Z$  denotes the vertical resolution. Whereas  $X$  represents the normalized signal following background subtraction, range correction, and overlap correction.  $\sigma_2$  denotes the extinction coefficient of air molecules.

### 3.2. SBDART model

The Santa Barbara DISORT Atmospheric Radiative Transfer (SBDART) model is founded on a set of well-established and dependable physical models, that have been created by the atmospheric science community over recent decades (Ricchiuzzi et al., 1998). This model is commonly employed to examine a range of radiative transfer issues faced in remote sensing and studies of the atmospheric energy budget (Bi et al., 2014, 2016; Li et al., 2023; Wang et al., 2020). To enhance the accuracy of radiative forcing simulations, we opted not to utilize certain default settings in SBDART. Instead, we updated the model's input parameters based on observational data. The automatic meteorological station measures SW (0.3–2.8  $\mu\text{m}$ ) and LW (4.5–42  $\mu\text{m}$ ) radiative flux, surface albedo, and location information. Additionally, the sun sky lunar photometer (Model CE318 T) captures AOD, AE, and WV metrics. The aerosol profile and atmospheric profile, including air density, specific humidity, temperature, and ozone, are obtained from lidar and reanalysis data (ERA5 and MERRA2). Hourly atmospheric profiles are constructed from reanalysis data and interpolated to match the height of aerosol profiles and time of ground observation. OMI delivers data on ozone column content. Single-scattering albedo (SSA) and asymmetry factor (ASY) are the statistical averages of dust aerosols across 13 AERONET sites in East Asia and Central Asia (Bi et al., 2016). The statistical results came from level 2.0 products, which only consider the case of  $\text{AOD}_{440\text{nm}} > 0.4$  and solar zenith angle  $> 50^\circ$  for smaller errors of SSA and ASY (Dubovik et al., 2000; Holben et al., 2006; Kaskaoutis et al., 2012). The retrieval errors of SSA and ASY are anticipated to be 0.03–0.05 and 0.04, relying on aerosol types and loading (Dubovik et al., 2000).

In this study, radiative forcing (RF) and heating rate (HR) are in the clear-sky condition. The computations are detailed below:

$$\Delta F = F_{\downarrow} - F_{\uparrow} \quad (5)$$

Where  $\Delta F$  denotes the net downward flux (downward minus upward radiation).

$$RF(\text{TOA}) = \Delta F^{\text{dust}}(\text{TOA}) - \Delta F^{\text{no}}(\text{TOA}) \quad (6)$$

$$RF(\text{SFC}) = \Delta F^{\text{dust}}(\text{SFC}) - \Delta F^{\text{no}}(\text{SFC}) \quad (7)$$

$$RF(\text{ATM}) = RF(\text{TOA}) - RF(\text{SFC}) \quad (8)$$

$$NRF = RF(\text{SW}) + RF(\text{LW}) \quad (9)$$

Where  $RF$  is the radiative forcing of dust aerosols.  $\text{TOA}$ ,  $\text{SFC}$ , and  $\text{ATM}$  respectively represent the top of the atmosphere, surface, and atmosphere. Note that *dust* and *no* indicate the conditions with and without dust aerosols.  $NRF$  is net radiative forcing,  $\text{SW}$  and  $\text{LW}$  represent shortwave and longwave.

$$DHR(z) = HR(z)^{\text{dust}} - HR(z)^{\text{no}} \quad (10)$$

Where  $DHR(z)$  and  $HR(z)$  denote the dust heating rate and heating rate at the height  $z$ .

The infrared temperature sensor was utilized to measure surface temperature within the wavelength range of 8–14  $\mu\text{m}$ , whereas the radiometer was employed to measure LW radiation flux spanning 4.5–42  $\mu\text{m}$ . Therefore, the observed temperature cannot be directly brought in SBDART, and the surface temperature needs to be used to correct it to  $T_{4.5-42 \mu\text{m}}$  (Zheng et al., 2019).

$$T_{4.5-42 \mu\text{m}} = \left[ \frac{Ra_{4.5-42 \mu\text{m}} - (1 - \varepsilon_g) Ra_{4.5-42 \mu\text{m}}}{\varepsilon_g \sigma} \right]^{\frac{1}{4}} \quad (11)$$

$Ra$  represents the radiation flux detected by the radiometer, while  $\varepsilon_g$  denotes the surface broadband emissivity. We refer to the study on

desert areas (Yalkun et al., 2019) and take  $\varepsilon_g$  as 0.88.  $\sigma$  is the Stefan-Boltzmann constant with a value of  $5.67 \times 10^{-8} \text{ W m}^{-2} \text{ K}^{-4}$ .

## 4. Results

### 4.1. Dust events at shaartuz in summer (2023)

In contrast to the common occurrence of dust events in northern China during the spring season, the dust events in Tajikistan in the summer are notably more intense, attributed to the limited precipitation in the region. After a series of corrections, we obtained ABC (Equation (1)) and VDR (Equation (2)) in the Summer of 2023. Fig. 2 illustrates the ABC, VDR of the lidar alongside the AOD and AE measurements from the sun sky lunar photometer at Shaartuz during the summer of 2023. Due to a power failure, certain data of the lidar was unavailable. The data shows that as the ABC (532 nm) increased, the high value of the VDR (greater than 0.2) suggests that the region was primarily influenced by irregular non-spherical particles. The daily averages of ABC and VDR varied from a background of  $1.4 \times 10^{-3} \text{ km}^{-1} \text{ sr}^{-1}$  and 0.13 to a maximum of  $4.3 \times 10^{-3} \text{ km}^{-1} \text{ sr}^{-1}$  and 0.24, respectively. The maximum dust height in June and July remained around 5 km and decreased slightly in August (3–4 km). The frequency of dust events at the site was high, with the intensity of dust aerosols in July surpassing that of the other two months. The results from the sun sky lunar photometer indicate that AOD and AE displayed contrasting trends, further confirming that Shaartuz has been subjected to dust aerosols for an extended period. The daily average  $\text{AOD}_{500\text{nm}}$  and  $\text{AE}_{440-870\text{nm}}$  ranged from 0.13 to 2.41 and 0.04 to 0.83, respectively. Total average  $\text{AOD}_{500\text{nm}}$  and  $\text{AE}_{440-870\text{nm}}$  in the summer of 2023 reached  $0.51 \pm 0.38$  (average  $\pm$  standard deviation) and  $0.34 \pm 0.15$ , respectively. The ABC of lidar demonstrated a strong correlation with the AOD measurements obtained from the sun sky lunar photometer. The extended duration of high-intensity dust aerosols would influence the redistribution of energy, resulting in changes to the atmospheric temperature profile and surface temperature.

### 4.2. Classification of dust levels

To facilitate the evaluation of the radiative impacts of dust aerosols

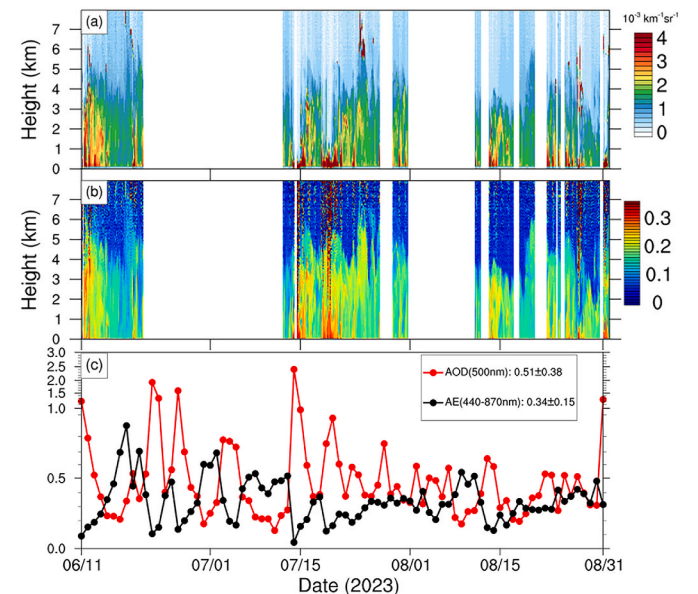


Fig. 2. Time evolutions of (a) attenuated backscatter coefficient ( $10^{-3} \text{ km}^{-1} \text{ sr}^{-1}$ ), (b) depolarization ratio from lidar measurements, and (c) the daily average of  $\text{AOD}_{500\text{nm}}$  and  $\text{AE}_{440-870\text{nm}}$  observed by sun sky lunar photometer at Shaartuz during the summer of 2023.

during the summer of 2023 in Shaartuz, we analyzed the continuity and quality of the AOD and AE data obtained from the sun sky lunar photometer, alongside the variations in dust structure detected by lidar. We categorized fifteen specific dust days into three classifications (adapted from Klüser and Schepanski, 2009): light dust ( $\text{AOD} < 0.3$ ,  $\text{AE} < 0.5$ ), moderate dust ( $0.3 < \text{AOD} < 0.5$ ,  $\text{AE} < 0.4$ ), and heavy dust ( $\text{AOD} > 0.5$ ,  $\text{AE} < 0.3$ ). Fig. 3 presents the observations of ABC, VDR, AOD, and AE as recorded by the lidar and sun sky lunar photometer throughout the five light dust days. The dust intensity near the ground, ranging from 0.2 to 0.6 km, was observed to be low, with daily averages for ABC and VDR recorded between  $1.5 \times 10^{-3}$  to  $1.7 \times 10^{-3} \text{ km}^{-1} \text{ sr}^{-1}$  and 0.14 to 0.16, respectively. However, the vertical height of dust aerosols could maintain stability at altitudes of 4–6 km over extended periods. AOD and AE were also relatively stable, with no significant fluctuations. The daily average of  $\text{AOD}_{500\text{nm}}$  and  $\text{AE}_{440-870\text{nm}}$  ranged from 0.19 to 0.29 and 0.24 to 0.46, and the total averages were 0.24 for  $\text{AOD}_{500\text{nm}}$  and 0.33 for  $\text{AE}_{440-870\text{nm}}$ . The results of the observation indicate that while the aerosol intensity over these five days was not exceptionally high, it exhibited characteristics of elevated aerosol layers, with the aerosol particles being coarse mode and irregularly shaped.

In comparison to light dust, the intensity of moderate dust (Fig. 4) showed a significant increase, with daily averages of ABC and VDR (0.2–0.6 km) rising from  $1.7 \times 10^{-3}$  to  $2.9 \times 10^{-3} \text{ km}^{-1} \text{ sr}^{-1}$  and 0.17 to 0.21, while the height remained consistent at 4–6 km. Observation of lidar reveals that dust aerosols exhibit multi-layered structures. For example, from 0:00–6:00 on July 17th, there were three distinct dust layers in the atmosphere: 0–0.8 km (the average of ABC and VDR were  $1.7 \times 10^{-3} \text{ km}^{-1} \text{ sr}^{-1}$  and 0.18), 1.2–2.5 km ( $1.9 \times 10^{-3} \text{ km}^{-1} \text{ sr}^{-1}$  and 0.18), and 2.7–3.4 km ( $1.6 \times 10^{-3} \text{ km}^{-1} \text{ sr}^{-1}$  and 0.19). Two distinct dust layers were observed from 15:20 to 24:00. The lower layer extends from 0 to 1.8 km, characterized by ABC of  $1.6 \times 10^{-3} \text{ km}^{-1} \text{ sr}^{-1}$  and VDR of 0.17. The higher layer ranges from 2.3 to 4 km, with ABC of 1.4

$\times 10^{-3} \text{ km}^{-1} \text{ sr}^{-1}$  and VDR of 0.17. Notably, the height of the higher layer shows a gradual decrease. The daily averages of  $\text{AOD}_{500\text{nm}}$  over the five days were recorded as 0.52, 0.37, 0.37, 0.38, and 0.32. The corresponding values for  $\text{AE}_{440-870\text{nm}}$  were 0.19, 0.33, 0.24, 0.29, and 0.17, respectively. The overall averages recorded were 0.39 for  $\text{AOD}_{500\text{nm}}$  and 0.24 for  $\text{AE}_{440-870\text{nm}}$ .

The intensity of dust extending from the ground to an altitude of 1 km was notably elevated during days of heavy dust (Fig. 5). The overall average values for ABC and VDR within the range of 0.2–0.6 km were recorded at  $2.6 \times 10^{-3} \text{ km}^{-1} \text{ sr}^{-1}$  and 0.20, respectively. The dust layers displayed multi-layered structures, with the uppermost layer positioned at an altitude of 4–6 km. For example, from 0:00–5:00 on July 15th, three distinct dust layers were identified in the atmosphere: the first layer ranged from 0 to 0.5 km, with an average of ABC and VDR measuring  $3.4 \times 10^{-3} \text{ km}^{-1} \text{ sr}^{-1}$  and 0.26; the second layer extended from 1.2 to 1.8 km, with values of  $2.2 \times 10^{-3} \text{ km}^{-1} \text{ sr}^{-1}$  and 0.23; and the third layer spanned from 2.3 to 3.4 km, recording  $1.4 \times 10^{-3} \text{ km}^{-1} \text{ sr}^{-1}$  and 0.24. The daily averages of  $\text{AOD}_{500\text{nm}}$  over the five days were recorded as 0.97, 0.59, 0.60, 0.58, and 0.58. The corresponding values for  $\text{AE}_{440-870\text{nm}}$  were 0.16, 0.21, 0.25, 0.19, and 0.13, respectively. The overall averages recorded were 0.67 for  $\text{AOD}_{500\text{nm}}$  and 0.19 for  $\text{AE}_{440-870\text{nm}}$ .

### 4.3. Radiative forcing and heating rate of dust aerosols

To assess the validity of the input parameters in the SBDART model, a radiative closure experiment is required (Bi et al., 2013; Ge et al., 2010; Huang et al., 2009). We compared the observed and simulated radiative fluxes during light, moderate, and heavy dust days, as shown in Fig. 6. Overall, the uncertainty of the simulation by SBDART was within a reasonable range, attributed to reliable station data and appropriate parameters. The  $R^2$  between the simulated and observed values of downward SW radiation achieved a value of 0.997. The Root Mean

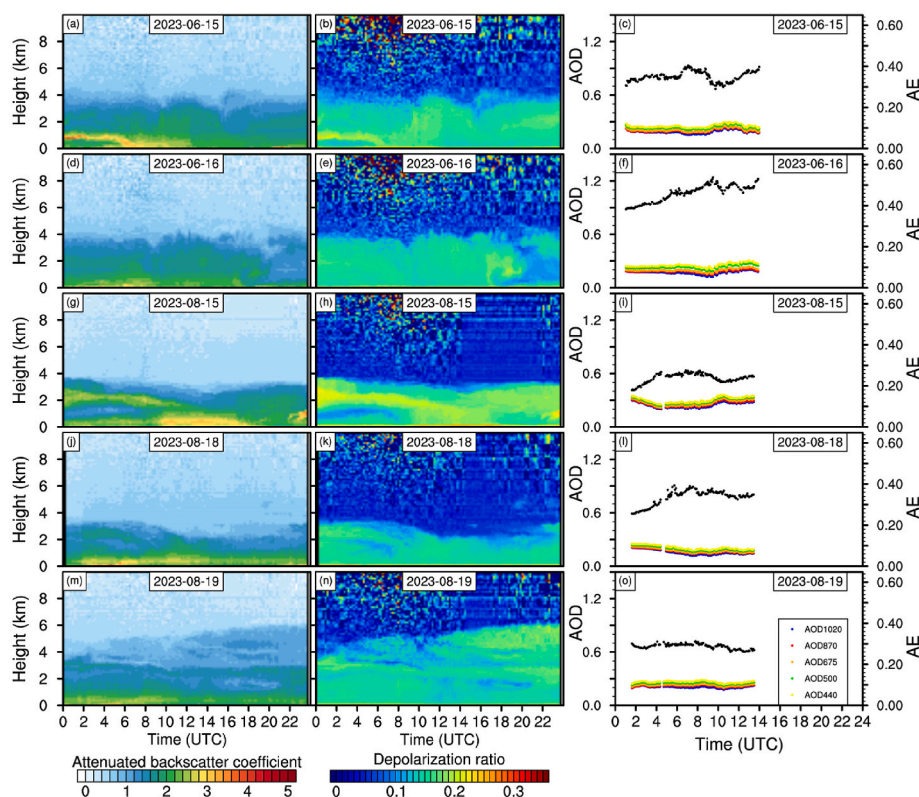


Fig. 3. Measurements of vertical structure and columnar aerosols optical properties observed by lidar and sun sky lunar photometer for selected light dust cases on June 15, June 16, August 15, August 18, and August 19, 2023, respectively.

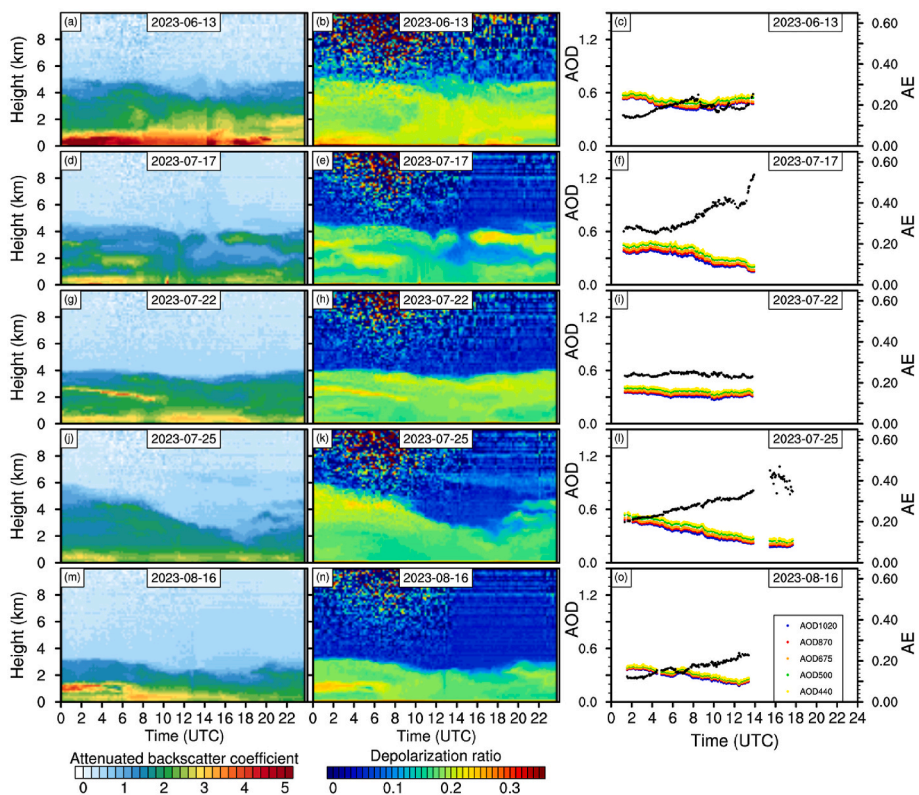


Fig. 4. Same as Fig. 3 but for moderate dust cases on June 13, July 17, July 22, July 25, and August 16, 2023, respectively.

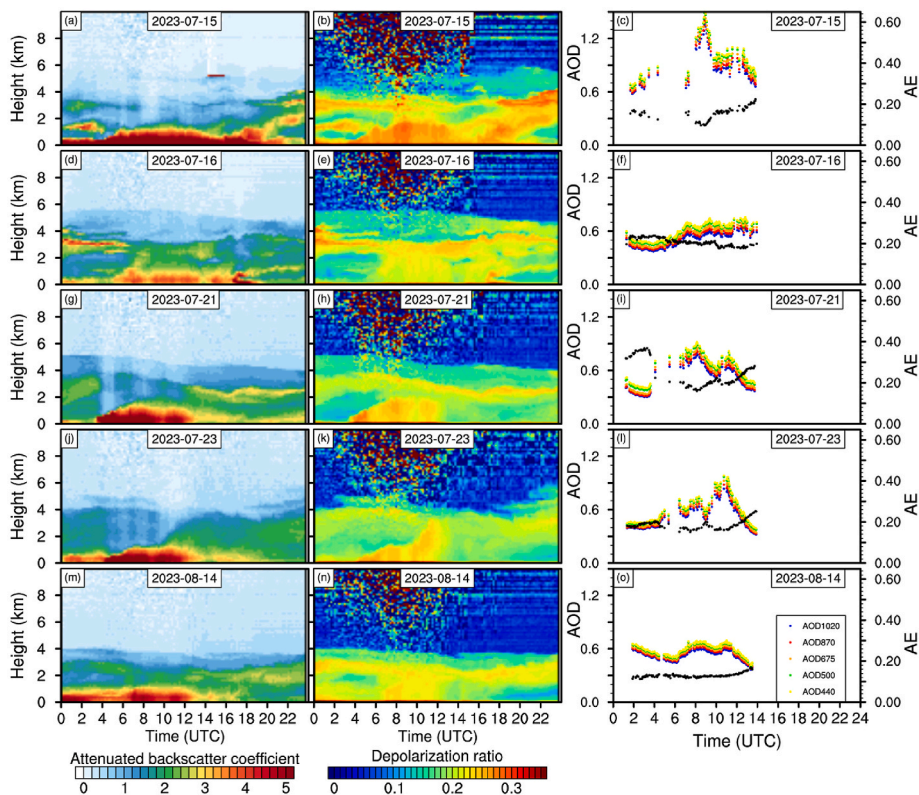
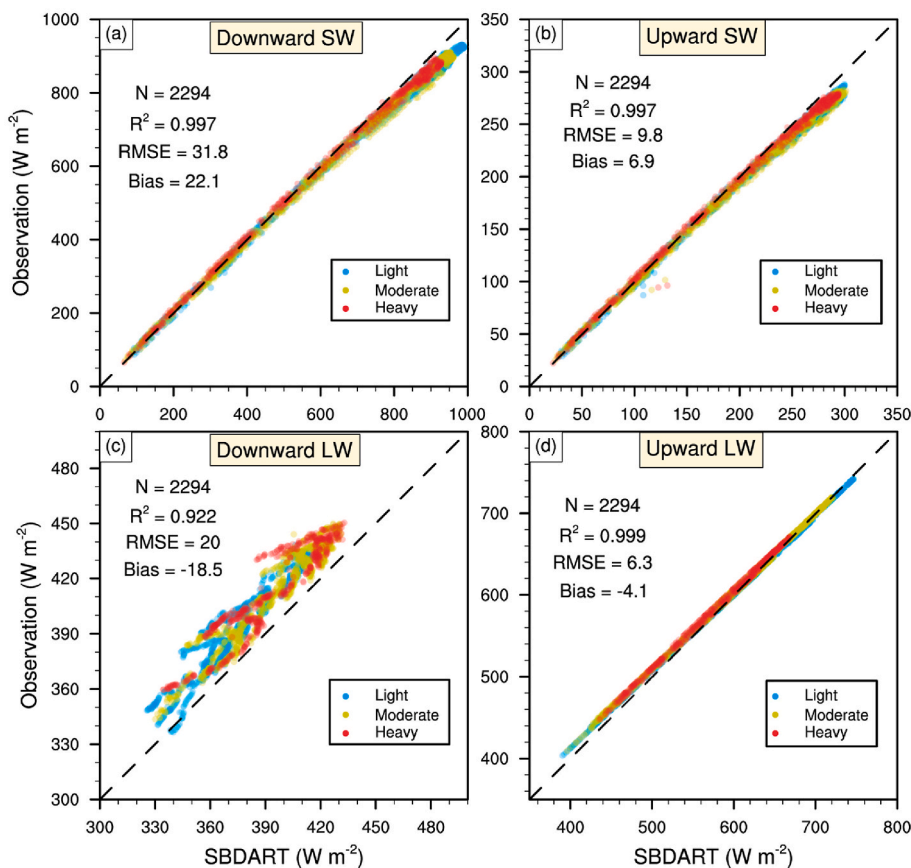


Fig. 5. Same as Fig. 3 but for heavy dust cases on July 15, July 16, July 21, July 23, and August 14, 2023, respectively.



**Fig. 6.** Comparison of radiative flux simulated by the SBDART model and observed by an automatic meteorological station system at Shaartuz, Tajikistan during the study period. Three different colored dots represent different levels of dust intensity.

Square Error (RMSE) was  $31.8 \text{ W m}^{-2}$ , with a Bias of  $22.1 \text{ W m}^{-2}$ . Specifically, the  $R^2$  and RMSE (Bias) for light dust were 0.9977 and  $35.8 (26.4) \text{ W m}^{-2}$ , for moderate dust were 0.9978 and  $31.8 (23.6) \text{ W m}^{-2}$ , and for heavy dust were 0.9979 and  $22.9 (11.9) \text{ W m}^{-2}$ . The simulation effect improved with increasing dust intensity, likely due to model's dust optical parameters (SSA, ASY) aligning more closely with the actual

conditions of heavy dust. The simulation of upward SW radiation at the surface exhibited similar characteristics. For light dust, the RMSE (Bias) was  $10.8 (8.3) \text{ W m}^{-2}$ , for moderate dust was  $9.9 (7.3) \text{ W m}^{-2}$ , and for heavy dust was  $7.6 (3.9) \text{ W m}^{-2}$ .  $R^2$  were similar, with values of 0.9974, 0.9974, and 0.9973, respectively. The overestimation of surface short-wave radiation by SBDART may be due to the AERONET statistical value

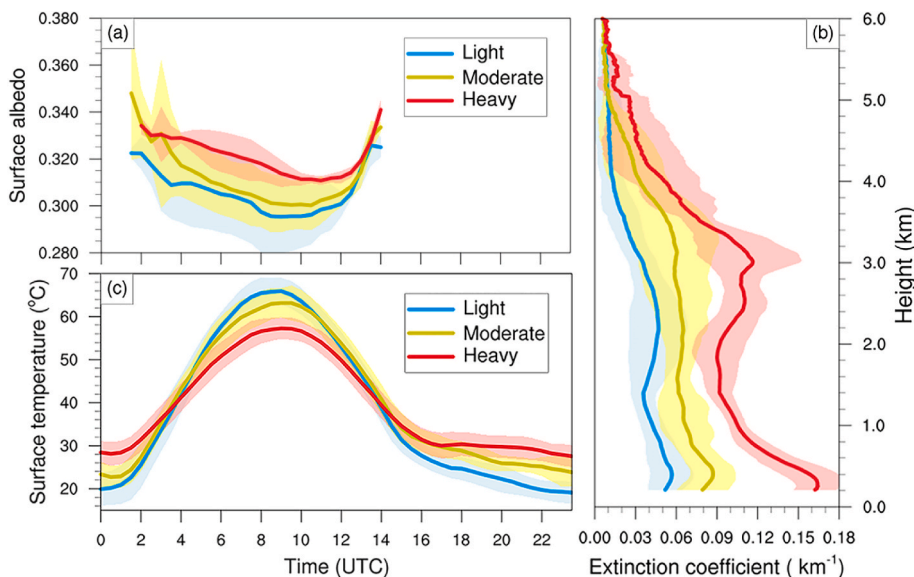


**Fig. 7.** Daily variations in (a) surface albedo, (b) vertical distribution of aerosol extinction coefficient, and (c) surface temperature under different levels of dust. The shaded areas represent the standard deviations.

overestimating the SSA of dust aerosols (Ge et al., 2011). The simulation of downward LW radiative flux at the surface was lower than the observed values, with an  $R^2$  of 0.922. The absence of real-time atmospheric profile observations led to inaccuracies in describing meteorological variables at Shaartuz based on reanalysis data; however, the overall error remained within an acceptable range. The RMSE was  $20.0 \text{ W m}^{-2}$ , with a Bias of  $-18.5 \text{ W m}^{-2}$ . Specifically, the  $R^2$  and RMSE (Bias) for light dust were 0.923 and  $19.9 (-18.6) \text{ W m}^{-2}$ , for moderate dust were 0.931 and  $18.7 (-17.4) \text{ W m}^{-2}$ , and for heavy dust were 0.874 and  $22.1 (-20.1) \text{ W m}^{-2}$ . These results suggest that the accuracy of the reanalysis data in describing the atmospheric profile for heavy dust days was lower than for light and moderate dust. Upon acquiring the corrected surface temperature (Equation (11)), the simulated and observed upward LW radiative flux values at the surface showed a high degree of consistency, with an  $R^2$  of 0.999. The RMSE was  $6.3 \text{ W m}^{-2}$ , and the Bias was  $-4.1 \text{ W m}^{-2}$ . Specifically, the  $R^2$  and RMSE (Bias) for light dust were 0.9997 and  $5.7 (-2.6) \text{ W m}^{-2}$ , as the intensity of sand and dust increases, the simulation error will slightly increase.

The strong alignment between the observed and simulated values demonstrates the dependability of the input parameters. The average parameters for three distinct dust conditions were calculated separately, as illustrated in Fig. 7. Fig. 7(a) illustrates that the surface albedo at Shaartuz was notably high during the summer, with an average value surpassing 0.32. Such a high surface albedo is comparable to that of a desert (Huang et al., 2009). It demonstrates a pattern of lower values in the afternoon (0.30–0.31) and higher values in the morning and at sunset (0.33–0.35). The daily variation of surface albedo exhibited a similar daily asymmetry to that of semi-arid grassland of the China's Loess Plateau (Zhu et al., 2024). The average surface albedo for heavy dust days was 0.33, which is higher than the values recorded for moderate and light dust days at 0.32. Fig. 7(b) illustrates the average vertical profile of the aerosol extinction coefficient based on daily measurements. The extinction coefficient is calculated based on Fernald's method (Equation (3) and 4) and a lidar ratio of 50 sr. Due to the blind area of the Lidar, we do not display information below 200 m. The extinction coefficient of heavy dust was found to be greater than that of moderate dust, which in turn was greater than that of light dust, with maximum values recorded at 0.16, 0.09, and  $0.06 \text{ km}^{-1}$  for the three levels, respectively. The average extinction coefficient profiles for light and heavy dust exhibited double-layer structures. The light dust layers were found at altitudes of 0–1 km, with maximum values reaching  $0.06 \text{ km}^{-1}$ , and at 1.5–3 km, with maximum values of  $0.05 \text{ km}^{-1}$ . In contrast, the heavy dust layers were observed at 0–1 km, where maximum values were  $0.16 \text{ km}^{-1}$ , and at 2–3.5 km, with maximum values of  $0.12 \text{ km}^{-1}$ . With the increase in height, the standard deviation of the extinction coefficient also showed an increase, suggesting notable variations in the distribution of dust within the upper layers. In order to align with the wavelength range of radiation flux, we corrected the surface temperature based on Equation (11). Fig. 7(c) illustrates that the daily variation of surface temperature displayed distinct characteristics depending on the intensity of dust. Dust aerosols could absorb and scatter solar SW radiation during daylight hours, thereby diminishing the amount of SW radiation that reaches the surface. Dust aerosols impede the outward escape of LW radiation, increasing the downward LW radiation that is reflected to the surface during both daytime and nighttime. The interaction of SW and LW radiation resulted in a reduction of surface temperature throughout the daytime, with the maximum surface temperature observed during heavy dust being  $8.6 \text{ }^\circ\text{C}$  lower than that recorded during light dust and  $5.9 \text{ }^\circ\text{C}$  lower than that during moderate dust. Conversely, at nighttime, the minimum surface temperature during heavy dust was  $8.5 \text{ }^\circ\text{C}$  higher than that of light dust and  $4.8 \text{ }^\circ\text{C}$  higher than that of moderate dust, thereby diminishing the temperature variation between daytime and nighttime.

Dust events were categorized according to their intensity, resulting in daily variations in surface albedo (Fig. 7(a)), surface temperature (Fig. 7(b)), and atmospheric profile (not shown in the figure) for light,

Table 1

The main variables input in the model under different levels of dust.

	AOD	AE	WV (g $\text{cm}^{-2}$ )	SSA	ASY
	440/675/ 870/1020 nm	440–870 nm		440/675/ 870/1020 nm	440/ 675/ 870/ 1020 nm
Light	0.26/0.22/ 0.20/0.19	0.34	1.31,	0.90/0.94/ 0.95/0.96	0.74/ 0.71/ 0.71/ 0.71
Moderate	0.41/0.37/ 0.35/0.33	0.24	1.71	0.90/0.94/ 0.95/0.96	0.74/ 0.71/ 0.71/ 0.71
Heavy	0.68/0.63/ 0.61/0.58	0.19	1.72	0.90/0.94/ 0.95/0.96	0.74/ 0.71/ 0.71/ 0.71
Uncertainty	0.01–0.02	/	<12%	0.03–0.05	0.04

moderate, and heavy dust intensities. Aerosol extinction coefficient profiles were also obtained (Fig. 7(c)), and other key input parameters were summarized in Table 1. To compute the 24-h continuous radiative forcing, we assume that aerosol remains relatively invariant during the entire day and interpolate the average aerosol parameters of daytime to the periods of missing data (including nighttime) to create a continuous time series. In Table 1, AOD, AE, and WV are the average values observed by the photometer at the Shaartuz under different dust

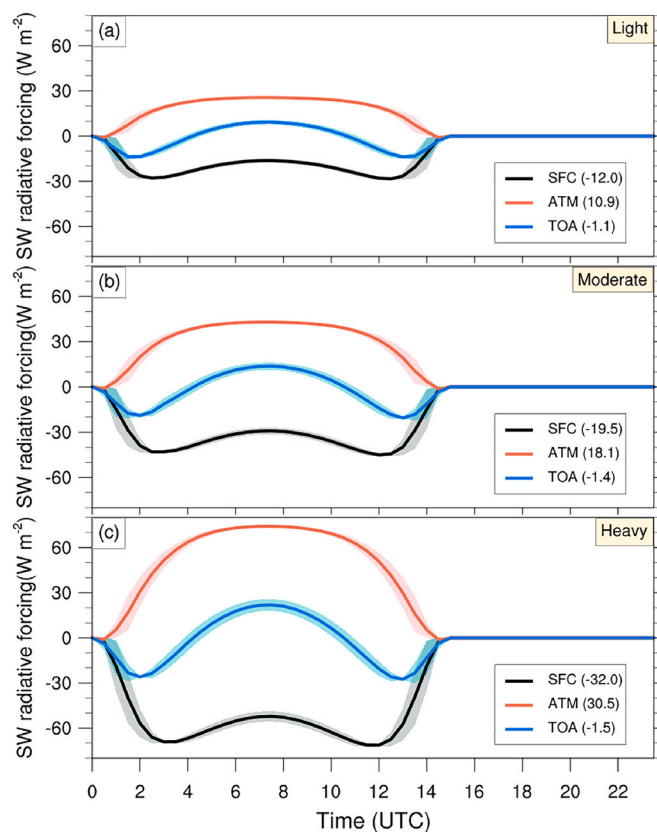


Fig. 8. Shortwave radiative forcing of dust aerosols under (a) light, (b) moderate, and (c) heavy dust, with black lines representing the surface (SFC), red representing the atmosphere (ATM), blue representing the top of the atmosphere (TOA), and shadows representing the standard deviation caused by changes in the position of the direct sunlight throughout the summer. (For interpretation of the references to color in this figure legend, the reader is referred to the Web version of this article.)

intensities, while SSA and ASY are the statistical averages of 13 sites in Asia (Bi et al., 2016). The radiative forcings were computed following Equation (5) to Equation (9) under the relevant conditions. Fig. 8 demonstrates that the absolute values of the daily average SW radiative forcing (SRF) exhibit an increase corresponding to the rise in dust intensity. The daily average SRF of dust aerosols at the surface was  $-12.0 \text{ W m}^{-2}$  for light dust,  $-19.5 \text{ W m}^{-2}$  for moderate dust, and  $-32.0 \text{ W m}^{-2}$  for heavy dust. In the atmosphere, the values were  $10.9 \text{ W m}^{-2}$  for light dust,  $18.1 \text{ W m}^{-2}$  for moderate dust, and  $30.5 \text{ W m}^{-2}$  for heavy dust. The daily average forcing at the TOA shows minimal variation, recorded at  $-1.1 \text{ W m}^{-2}$  for light dust,  $-1.4 \text{ W m}^{-2}$  for moderate dust, and  $-1.5 \text{ W m}^{-2}$  for heavy dust. The daily variation trend of the SRF of dust aerosols exhibited consistency, with the surface SRF consistently remaining negative. Its absolute value demonstrated a pattern of being larger in the morning and during sunset compared to noon. It indicated that SRF in the atmosphere consistently remained positive, progressively rising from the morning hours until approximately 7:00 (local time around 12:00 noon), at which point it attained its peak value before commencing a decline. The observed variation resulted from changes in the zenith angle of the sun. The morning and sunset experienced negative forcing at the top of the atmosphere, while noon exhibited positive forcing, leading to a daily mean that was a small negative value.

Fig. 9 depicts the LW radiative forcing (LRF) of dust aerosols, which shows a gradual increase after sunrise, peaks at noon, and subsequently declines. The surface and top of the atmosphere exhibited positive forcing, which intensified alongside the increase in dust intensity. Under light, moderate, and heavy dust conditions, the surface radiative forcing values were  $4.1 \text{ W m}^{-2}$ ,  $7.6 \text{ W m}^{-2}$ , and  $13.8 \text{ W m}^{-2}$ . The corresponding values at the top of the atmosphere (TOA) were  $3.4 \text{ W m}^{-2}$ ,  $6.4 \text{ W m}^{-2}$ , and  $11.1 \text{ W m}^{-2}$ , respectively. The LRFs of dust aerosols in the atmosphere exhibited small negative values due to the absorption of energy by dust aerosols, which subsequently emitted LW radiation into outer

space, thereby diminishing the original LW radiation present in the atmosphere. The result indicates that for the atmosphere, the absolute value of LRF was considerably lower than SW forcing. However, at the TOA, the LW radiative effect was more pronounced than SW. The surface heating from LW radiation compensated for 34.2%, 39.0%, and 43.1% of SW cooling in light, moderate, and heavy cases, respectively. At the top of the atmosphere, the heating from LRF was 309.1%, 457.1%, and 740.0% of SRF, highlighting the significance of LRF at both the surface and the top of the atmosphere. While the surface experienced a predominant cooling effect during the day, the SRF was zero at night. The persistence of LRF would elevate nighttime surface temperatures, consequently diminishing the diurnal temperature variation.

Fig. 10(a), (b), and (c) illustrates the net radiative forcing (NRF) of dust aerosols under light, moderate, and heavy conditions, respectively. The daily variation of NRF during the daytime was primarily influenced by SW, whereas at night, it was predominantly governed by LW. The presence of dust aerosols resulted in a cooling effect on the surface, with NRF values recorded at three different intensities:  $7.9 \text{ W m}^{-2}$ ,  $-12.0 \text{ W m}^{-2}$ , and  $-18.2 \text{ W m}^{-2}$ , respectively. The heating of the atmosphere produced NRF values of  $10.2 \text{ W m}^{-2}$ ,  $16.9 \text{ W m}^{-2}$ , and  $27.7 \text{ W m}^{-2}$  at three distinct intensities, respectively. At the TOA, heating effects were recorded at  $2.3 \text{ W m}^{-2}$ ,  $5.0 \text{ W m}^{-2}$ , and  $9.6 \text{ W m}^{-2}$ , respectively. The substantial variations in dust intensity across various cases and regions render direct comparisons of forcing values inaccurate. Consequently, numerous studies have presented the concept of net radiative forcing efficiency (NRFE). NRFE is calculated as the net radiative forcing divided by the corresponding  $\text{AOD}_{500\text{nm}}$  of dust aerosols. Fig. 10(d) demonstrates that the daily fluctuation of NRFE aligned with the fluctuation of NRF. The daily average efficiency is  $-30.2 \text{ W m}^{-2} \text{ AOD}^{-1}$  at the surface,  $42.5 \text{ W m}^{-2} \text{ AOD}^{-1}$  in the atmosphere, and  $12.3 \text{ W m}^{-2} \text{ AOD}^{-1}$  at the TOA. The analysis shows that the heating impact of dust aerosols in the atmosphere surpassed the cooling effect at the surface, leading to a net heating effect of dust aerosols on the Earth's atmospheric system in this area. The conclusion was made based on the surface albedo, along with the absorption and scattering characteristics of dust aerosols. The shadow illustrates the standard deviation of three intensities. It indicates that, following division by AOD, the variation in NRFE among the three intensities was marginally greater during sunrise and sunset, while remaining insignificant at other times.

Previous studies (Chen et al., 2024; Claquin et al., 1998; Kok et al., 2023; Liao and Seinfeld, 1998) indicate that when dust aerosols are positioned over high-albedo surfaces, such as deserts and snow, the warming effect of SW absorption is enhanced. Conversely, when dust aerosols are positioned over low-albedo surfaces, such as forests and oceans, the cooling effect from SW scattering is amplified. In these cases, the majority of radiation is reflected into space, whereas on high-albedo surfaces, more radiation is absorbed. This explains why some studies (Filonchik et al., 2021, 2024; Li et al., 2004; Peris et al., 2017) suggest that dust aerosols contribute to a cooling effect at TOA. From Table 2, it is evident that the absolute value of dust radiative forcing efficiency at the surface of Shaartuz is lower than in other regions, indicating that the cooling effect of dust aerosols at the surface is smaller than in the Taklamakan Desert (Huang et al., 2009), the Mediterranean (Meloni et al., 2015), Lahore (Alam et al., 2014), and Patiala (Sharma et al., 2012) in South Asia. The radiative forcing efficiency in the atmosphere is greater than in the Mediterranean, comparable to that in South Asia, and smaller than in the Taklamakan Desert. The surfaces of the Mediterranean, Lahore, and Patiala are darker, resulting in a negative radiative forcing efficiency for dust aerosols at the TOA. In contrast, the surfaces of the Taklamakan Desert and Shaartuz are brighter, and the radiative forcing efficiency at the TOA is positive, indicating that dust plays a warming role in the Earth's atmospheric system in these regions. Due to differences in statistical methods, we will not discuss other studies in detail. However, it is clear that in bright surface areas of West Africa, the radiative forcing efficiency at the TOA is positive (Saidou Chaibou et al., 2020), while in other darker surface areas, it is negative

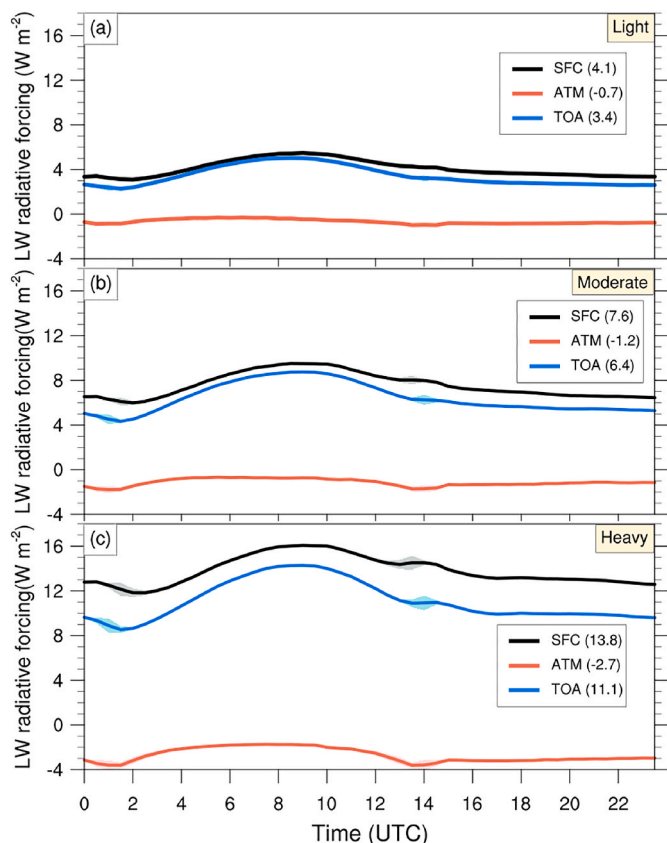
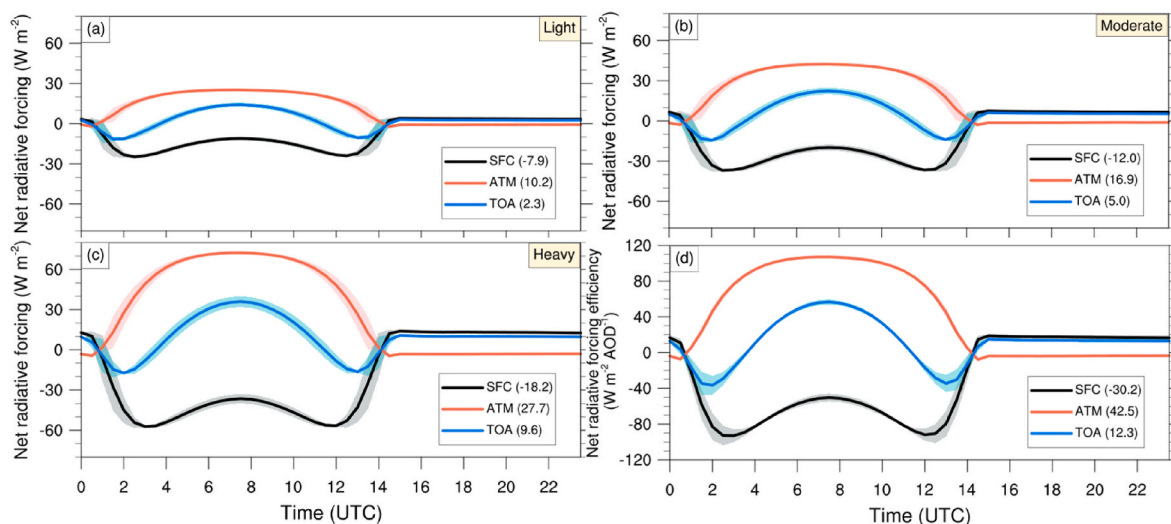


Fig. 9. Same as Fig. 8 but for longwave radiative forcing.



**Fig. 10.** The net radiative forcing of dust aerosols is illustrated under three conditions: (a) light, (b) moderate, and (c) heavy dust. The black lines denote the surface (SFC), red indicates the atmosphere (ATM), blue represents the top of the atmosphere (TOA), and the shadows reflect the standard deviation resulting from variations in the position of direct sunlight during the summer. (d) The net radiative forcing efficiency. The shadows indicate the standard deviation across varying intensities: light, moderate, and heavy. (For interpretation of the references to color in this figure legend, the reader is referred to the Web version of this article.)

**Table 2**

Comparison of dust net radiative forcing efficiency ( $\text{W m}^{-2} \text{AOD}^{-1}$ ) between the present and previous studies (For consistency in comparison, the results of the studies were uniformly processed into net radiative forcing efficiency). SFC: surface. ATM: atmosphere. TOA: top of the atmosphere. 'Points' represents the average of valid data points. 'Inst.' represents instantaneous value. 'Integ.' represents integrating the instantaneous values.

Location		SFC	ATM	TOA	SSA 675 nm	Surface albedo	References
Taklimakan	Daily	-56	108	53	0.89	0.346	Huang et al. (2009)
Mediterranean	Daily	-84	25	-59	/	0.09 to 0.15	Meloni et al. (2015)
Lahore	Daily	-80	46	-35	0.98	/	Alam et al. (2014)
Patiala	Daily	-67	52	-15	/	0.15	Sharma et al. (2012)
<b>Tajikistan</b>	<b>Daily</b>	<b>-30</b>	<b>43</b>	<b>12</b>	<b>0.94</b>	<b>0.32 to 0.34</b>	<b>This study</b>
Baotou	Points	-206	151	-55	0.98	/	Filonchik et al. (2024)
West Africa	Summer	-19	33	13	/	/	Saidou Chaibou et al. (2020)
Mediterranean	Inst.	-112	48	-64	/	0.07	Di Sarra et al. (2011)
Mediterranean	Points	-164	138	-26	/	0.06	Peris et al. (2017)
Barcelona	Points	-74	50	-24	/	0.018	Sicard et al. (2014)
Evora	Integ.	-103	53	-50	0.96	/	Valenzuela et al. (2017)

(Di Sarra et al., 2011; Peris et al., 2017; Sicard et al., 2014; Valenzuela et al., 2017). These findings confirm the conclusion of Liao and Seinfeld (1998) that the heating or cooling effect of dust aerosols on the Earth's atmospheric system largely depends on the surface albedo.

The SRF of dust aerosols in the atmosphere has been established as a significant positive forcing, leading to atmospheric heating. The LRF represented a comparatively weak negative forcing, as previously outlined. The vertical heating rate of dust aerosols was determined by the difference between the presence and absence of dust (Equation (10)). We use the aerosol extinction coefficient profile in Fig. 7(b) to represent the vertical distribution of dust. Fig. 11 illustrates the shortwave heating rate (SHR) of dust aerosols across three distinct scenarios. The vertical distributions observed align with the extinction coefficient profiles presented in Fig. 7(b), demonstrating double-layer structures under both light and heavy dust conditions. During conditions of heavy dust, the heating rate near ground level surpassed  $2 \text{ K day}^{-1}$ , whereas the heating rate attained  $1.5 \text{ K day}^{-1}$  at altitudes ranging from 2.5 to 3.5 km. The peak values of SHR under the three conditions are 0.7, 1.1, and  $2.1 \text{ K day}^{-1}$ , respectively. The presence of dust aerosols was shown to absorb solar SW radiation, leading to atmospheric heating. This phenomenon can influence local weather and climate by altering the thermal and dynamic structure of the atmosphere (Chen et al., 2023; Victor et al., 2024).

The longwave heating rate (LHR) in Fig. 12 was significantly lower

than SHR, aligning with the findings related to radiative forcing in the atmosphere. The maximum LHR are 0.05, 0.10, and  $0.14 \text{ K day}^{-1}$  for light, moderate, and heavy dust conditions, respectively. It illustrates the heating characteristics in the lower layer (0–2 km) and the cooling effects observed in the upper layer (2–6 km). The vertical distribution can be attributed to the high surface temperature and the multi-layered configuration of dust aerosols. Considering diurnal variation, the LW heating exhibited its greatest intensity in the lower layer at noon, whereas the cooling was most pronounced in the upper layer (3–4 km) during the morning and at nightfall. The influence of LHR on the net radiative heating rate was small during daylight hours. However, once SHR was lost, LHR persisted in impacting the atmospheric thermal structure during the night.

#### 4.4. Uncertainties in radiative forcing and heating rate

In Sections 2 and 3, we discussed the uncertainty associated with the input parameters. We referenced the methods proposed by Huang et al. (2009) and Wang et al. (2020) for assessing uncertainty and conducted sensitivity tests on SSA, ASY, and WV, as these parameters significantly impact the simulation of radiative forcing and heating rate. In Tables 3 and 4, we examine the potential errors in radiative forcing and heating rate resulting from uncertainties in these three parameters under heavy dust. The observation error of AOD is relatively small (0.01–0.02, Eck

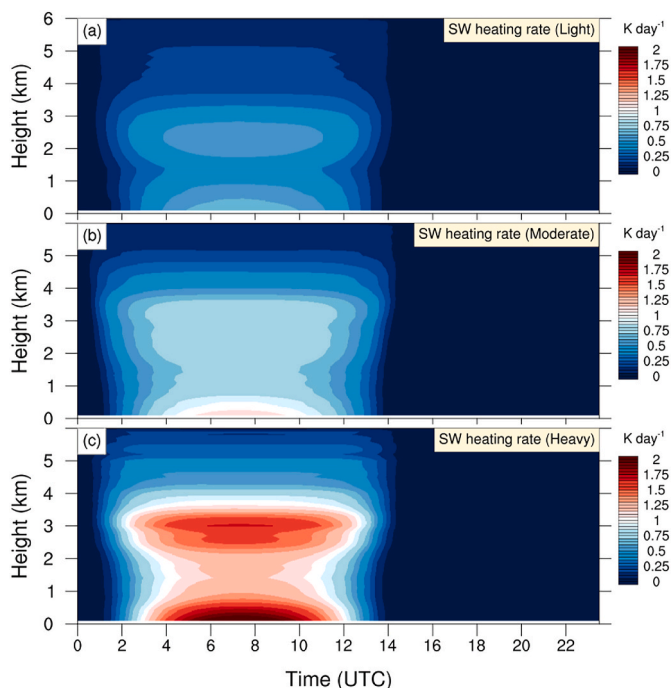


Fig. 11. The shortwave heating rate of dust aerosols under (a) light, (b) moderate, and (c) heavy dust.

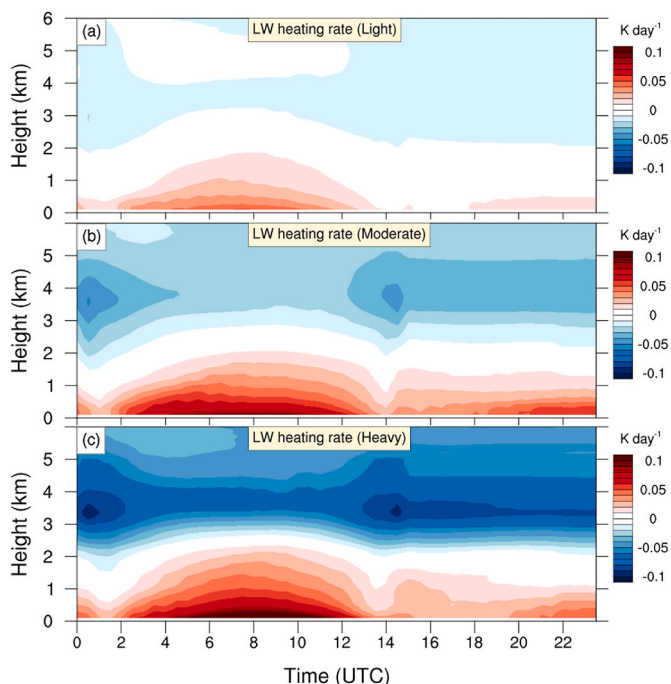


Fig. 12. The longwave heating rate of dust aerosols under (a) light, (b) moderate, and (c) heavy dust.

Table 3  
Estimation of uncertainties of radiative forcing. Unit:  $W m^{-2}$ .

	SFC			ATM			TOA		
	SW	LW	NET	SW	LW	NET	SW	LW	NET
SSA±4%	±10.9	∓2.3	±8.6	∓22.6	±2.0	∓20.5	∓11.7	∓0.2	∓11.9
ASY±5%	±3.0	∓1.7	±1.3	∓0.3	±0.2	∓0.1	±2.7	∓1.5	±1.2
WV±12%	±0.1	∓1.1	∓1.0	∓0.1	±0.3	±0.1	±0.0	∓0.8	∓0.8

et al., 1999; Holben et al., 1998) and is not discussed further here. The errors in SSA and ASY from the 13 AERONET stations arise from the inversion algorithm, with uncertainties ranging from 0.03 to 0.04 and 0.04, respectively (Bi et al., 2016; Dubovik et al., 2000). Consequently, we assume their uncertainties to be 4% and 5%, while the inversion uncertainty for WV is assumed to be 12% (Holben et al., 1998). As shown in Table 3, the uncertainty in SSA leads to significant variation in the simulation of shortwave radiative forcing (SRF) and heating rate, with an error of  $22.6 W m^{-2}$  for the atmosphere and  $0.2182 K day^{-1}$  for the average SHR. In contrast, the impact of ASY is much smaller, causing a maximum error of  $3.0 W m^{-2}$  in surface SRF and  $0.003 K day^{-1}$  in the average SHR. The inversion error for WV primarily introduces uncertainty in longwave radiation, contributing a maximum uncertainty of  $1.1 W m^{-2}$  in longwave radiative forcing (LRF) at the surface and  $0.002 K day^{-1}$  in the average LHR. It should be noted that the sensitivity tests presented here represent the theoretical maximum uncertainty resulting from parameter inversion errors and do not reflect the actual uncertainty of our results.

### 5. Conclusions

We assessed the radiative forcing of dust aerosols and the vertical heating rate at Shaartuz during the summer of 2023 utilizing the sun sky lunar photometer, dual-wavelength polarization Raman lidar, and the SBDART model. The primary input parameters of the model consist of aerosol optical parameters such as AOD, AE, SSA, and ASY, along with vertical profiles of the aerosol extinction coefficient, atmospheric temperature, humidity, ozone, and other relevant factors. The findings indicate that the occurrence of dust events in this region was notably high, with dust aerosol layers consistently observed at altitudes of 4–6 km throughout the observation period. These layers exhibited multi-layered structures, which exceed the height of the dust stagnation layer found in the interior of the Taklamakan Desert (Bi et al., 2022). The overall average  $AOD_{500nm}$  and  $AE_{440-870nm}$  at Shaartuz were measured at  $0.51 ± 0.38$  and  $0.34 ± 0.15$ , respectively, indicating the dominance of coarse dust particles throughout the entire observation period. Using the AOD and AE, we categorized the dust days into three classifications: light, moderate, and heavy dust. The mean values of  $AOD_{500nm}$  across the three scenarios are 0.24, 0.39, and 0.67, respectively. The aerosol average extinction coefficient reached maximum values of  $0.06 ± 0.02$ ,  $0.09 ± 0.02$ , and  $0.16 ± 0.02 km^{-1}$  at heights ranging from 255 to 420 m for light, moderate, and heavy dust, respectively. A notable dust layer was identified at an altitude of 2–3.5 km beneath heavy dust, with the extinction coefficient measured at 3 km reaching  $0.12 ± 0.04 km^{-1}$ .

The daily average SRF of dust aerosols was measured at  $-12.0$ ,  $-19.5$ , and  $-32.0 W m^{-2}$  at the surface,  $10.9$ ,  $18.1$ , and  $30.5 W m^{-2}$  in

Table 4  
Estimation of uncertainties of vertical averaged atmospheric heating rate. Unit:  $K day^{-1}$ .

	SW	LW	NET
SSA±4%	∓0.2182	±0.0180	∓0.2003
ASY±5%	∓0.0025	±0.0004	∓0.0021
WV±12%	∓0.0012	±0.0017	±0.0005

the atmosphere, and  $-1.1$ ,  $-1.4$ , and  $-1.5 \text{ W m}^{-2}$  at TOA, corresponding to light, moderate, and heavy dust conditions, respectively. These results are smaller than the findings from Huang et al. (2009) on the dust in the Taklamakan Desert. The daily averages of LW radiative heating at the surface compensated for 34.2%, 39.0%, and 43.1% of SW cooling under the three conditions, while at the TOA, the heating of LW radiation were 309.1%, 457.1%, and 740.0% of SW cooling, respectively. This highlights the importance of longwave radiative forcing (LRF) in net radiation effects and confirms that large dust particles significantly influence longwave radiation. The NRFE at the surface consistently exhibited negative values during the daytime, attributed to the influence of SRF, while at night, it showed positive values due to LRF, resulting in a daily average of  $-30.2 \text{ W m}^{-2} \text{ AOD}^{-1}$ . The NRFE in the atmosphere consistently exhibited positive values during daylight hours as a result of SW absorption, while at night, it showed weakly negative values attributed to LRF. The daily average was  $42.5 \text{ W m}^{-2} \text{ AOD}^{-1}$ . The results at the TOA indicated a negative value for several hours surrounding both sunrise and sunset while remaining positive during the remainder of the day. The peak value was recorded at noon, resulting in a daily average of  $12.3 \text{ W m}^{-2} \text{ AOD}^{-1}$  at the TOA. The high surface albedo (0.30–0.35) observed at Shaartuz led to positive SRF values at the TOA during daylight hours. This, combined with the effects of LRF, resulted in positive daily averages of NRF at the TOA. These results are consistent with those from the Taklamakan Desert (Huang et al., 2009) and the Sahara Desert (Saidou Chaibou et al., 2020), but opposite to findings over oceans (Meloni et al., 2015) and urban areas (Alam et al., 2014; Sharma et al., 2012), primarily due to differences in surface albedo. Liao and Seinfeld (1998) noted that as surface albedo increases, the SRF of dust aerosols at the TOA can transition from negative to positive, altering net radiative forcing. When surface albedo is constant, decreasing SSA (i.e., increased dust particle absorption) results in a transition from negative to positive radiative forcing (Huang et al., 2014). This underscores the importance of accurately characterizing the optical properties of dust aerosols and surface conditions in studies of dust radiative effects. In Section 4.4, we discussed how the uncertainty in SSA is a major source of error in evaluating dust radiative effects. The SSA of dust aerosols is influenced by particle composition (Sokolik and Toon, 1999), size (Su and Toon, 2011), and other factors. The aggregation of hematite with quartz or clays can significantly enhance SW absorption by dust (Sokolik and Toon, 1999). Small particles (0.1–1.0  $\mu\text{m}$  in diameter) have larger scattering and absorption cross-sections per unit mass than larger particles (Steinfeld, 1998). Studies show that the SSA of East Asian dust is higher than that of Sahara dust (Su and Toon, 2011), and anthropogenic aerosol pollution in urban areas can reduce the SSA of dust (Ge et al., 2010; Pandithurai et al., 2008). Therefore, to better understand the role of dust aerosols in climate change, ongoing development of regional and global dust optical parameter observation programs is essential.

The results of radiative forcing indicate that dust aerosols in the atmosphere have a significant heating effect. We conducted a detailed analysis of the vertical heating rate of dust aerosols by analyzing the aerosol extinction coefficient profile. The findings indicate that the heating rate of dust aerosols in the atmosphere was predominantly influenced by SW heating, with LW values being significantly lower than SW values. The SHR of dust aerosols below 500 m were  $0.7 \text{ K day}^{-1}$  for light dust,  $1.1 \text{ K day}^{-1}$  for moderate dust, and  $2.1 \text{ K day}^{-1}$  for heavy dust. Under conditions of heavy dust, the heating rate attained  $1.7 \text{ K day}^{-1}$  at altitudes of 3 km. The original atmospheric thermal structure and surface temperature of the region were significantly altered. During heavy dust conditions, the highest surface temperature was recorded at  $8.6 \text{ }^\circ\text{C}$  lower than that of light dust and  $5.9 \text{ }^\circ\text{C}$  lower than that of moderate dust. How the dual heating structure and surface cooling under heavy dust affected regional atmospheric circulation and how they further affected the climate characteristics of the region is a goal for the future research. To the best of our knowledge, this is the first study of dust aerosol vertical profiles and heating rates in southwestern

Tajikistan. The findings contribute to understanding the influence of dust aerosols on the regional energy budget and their interactions with precipitation in Central Asia.

#### CRediT authorship contribution statement

**Zhengpeng Li:** Writing – original draft, Visualization, Software, Methodology, Investigation. **Zhongwei Huang:** Writing – review & editing, Resources, Project administration, Funding acquisition, Formal analysis, Conceptualization. **Jianrong Bi:** Writing – review & editing, Validation, Investigation, Funding acquisition, Conceptualization. **Qingqing Dong:** Validation, Methodology. **Yongkai Wang:** Resources, Investigation. **Sabur F. Abdullaev:** Resources, Project administration, Investigation. **Dilovar Nozirov:** Resources, Project administration, Investigation. **Wuren Li:** Investigation, Data curation. **Ze Li:** Investigation, Data curation. **Zhaozhao Meng:** Investigation, Data curation. **Wentao Liu:** Investigation, Data curation. **Xiaodong Song:** Investigation, Data curation.

#### Data Availability Statement

The data of Land Cover Type is available via the Land Processes Distributed Active Archive Center (LP DAAC, <https://lpdaac.usgs.gov/products/mcd12c1v061/>). SBDART model can be downloaded and installed from the following website: <https://github.com/paulricchiazzi/SBDART>. The ozone column content of input parameters in the model can be obtained through [https://acdisc.gesdisc.eosdis.nasa.gov/data/Aura\\_OMI\\_Level3/OMSO2e.003/](https://acdisc.gesdisc.eosdis.nasa.gov/data/Aura_OMI_Level3/OMSO2e.003/). Atmospheric vertical profile (air density, specific humidity, temperature, ozone) in the model can be derived from ERA5 (<https://cds.climate.copernicus.eu/datasets/reanalysis-era5-pressure-levels?tab=download>) and MERRA2 (<https://goldsmr5.gesdisc.eosdis.nasa.gov/data/MERRA2/M2I3NVCH/M.5.12.4/>). All requests for observation data (sun sky lunar photometer, lidar, the automatic meteorological station) used in this study can be available on request. The last access of the above websites: October 11, 2024.

#### Declaration of competing interest

The authors declare that they have no known competing financial interests or personal relationships that could have appeared to influence the work reported in this paper.

#### Acknowledgments

This work is jointly supported by the National Natural Science Foundation of China (W2411029), the Gansu Science and Technology Major Program (24ZDWA006) and the Fundamental Research Funds for the Central Universities (lzujbky-2024-jdxx04). The authors would like to express special thanks to Earth Space Research Group, Institute for Computational Earth System Science, University of California, Santa Barbara for the contribution to the SBDART model used in this study. We are grateful to the MODIS, OMI, ERA5, and MERRA2 teams for supplying the satellite data and reanalysis products used in this study. We also appreciate the editors and all anonymous reviewers for their insightful and valuable comments.

#### Data availability

I have shared the link to my data at the Data Availability Statement.

#### References

- Abdullaev, S.F., Sokolik, I.N., 2019. Main characteristics of dust storm sand their radiative impacts: with a focus on Tajikistan. *Journal of Atmospheric Science Research* 2, 1–21. <https://doi.org/10.30564/jasr.v2i2.352>.

- Abdullaev, S.F., Nazarov, B.I., Maslov, V.A., Djuraev, A.A., 2013. Distribution of natural and anthropogenic radioactivity in samples of soil and dust haze in the south of Tajikistan. *Atmospheric and Oceanic Optics* 26, 396–403. <https://doi.org/10.1134/S1024856013050023>.
- Alam, K., Trautmann, T., Blaschke, T., Subhan, F., 2014. Changes in aerosol optical properties due to dust storms in the Middle East and Southwest Asia. *Remote Sensing of Environment* 143, 216–227. <https://doi.org/10.1016/j.rse.2013.12.021>.
- Barreto, A., Cuevas, E., Damiri, B., Guirado, C., Berkoff, T., Berjón, A.J., Hernández, Y., Almansa, F., Gil, M., 2013. A new method for nocturnal aerosol measurements with a lunar photometer prototype. *Atmos. Meas. Tech.* 6, 585–598. <https://doi.org/10.5194/amt-6-585-2013>.
- Bi, J., Huang, J., Fu, Q., Ge, J., Shi, J., Zhou, T., Zhang, W., 2013. Field measurement of clear-sky solar irradiance in badain jaran desert of northwestern China. *J. Quant. Spectrosc. Radiat. Transf.* 122, 194–207. <https://doi.org/10.1016/j.jqsrt.2012.07.025>.
- Bi, J., Huang, J., Holben, B., Zhang, G., 2016. Comparison of key absorption and optical properties between pure and transported anthropogenic dust over East and Central Asia. *Atmos. Chem. Phys.* 16, 15501–15516. <https://doi.org/10.5194/acp-16-15501-2016>.
- Bi, J., Huang, J., Hu, Z., Holben, B.N., Guo, Z., 2014. Investigating the aerosol optical and radiative characteristics of heavy haze episodes in Beijing during January of 2013. *J. Geophys. Res.* Atmos. 119, 9884–9900. <https://doi.org/10.1002/2014JD021757>.
- Bi, J., Li, B., Ma, J., Wang, X., Meng, Z., Shi, J., Li, Z., 2024. Evaluation of nocturnal aerosol optical depth determining from a lunar photometry in Lanzhou of northwest China. *J. Geophys. Res.* Atmos. 129, e2023JD040387. <https://doi.org/10.1029/2023JD040387>.
- Bi, J., Li, Z., Zuo, D., Yang, F., Li, B., Ma, J., Huang, Z., He, Q., 2022. Dust aerosol vertical profiles in the hinterland of Taklimakan Desert during summer 2019. *Front. Environ. Sci.* 10, 851915. <https://doi.org/10.3389/fenvs.2022.851915>.
- Chen, A., Zhao, C., Zhang, H., Yang, Y., Li, J., 2024. Surface albedo regulates aerosol direct climate effect. *Nat. Commun.* 15, 7816. <https://doi.org/10.1038/s41467-024-52255-z>.
- Chen, Y., Chen, S., Zhou, J., Zhao, D., Bi, H., Zhang, Y., Alam, K., Yu, H., Yang, Y., Chen, J., 2023. A super dust storm enhanced by radiative feedback. *npj Climate and Atmospheric Science* 6, 90. <https://doi.org/10.1038/s41612-023-00418-y>.
- Claquin, T., Michael, S., Balkanski, Y., Boucher, O., 1998. Uncertainties in assessing radiative forcing by mineral dust. *Tellus B* 50, 491–505. <https://doi.org/10.1034/j.1600-0889.1998.t01-2-00007.x>.
- Di Sarra, A., Di Biagio, C., Meloni, D., Monteleone, F., Pace, G., Pugnaghi, S., Sferlazzo, D., 2011. Shortwave and longwave radiative effects of the intense Saharan dust event of 25–26 March 2010 at Lampedusa (Mediterranean Sea). *J. Geophys. Res.* Atmos. 116, 23209. <https://doi.org/10.1029/2011JD016238>.
- Dong, Q., Huang, Z., Li, W., Li, Z., Song, X., Liu, W., Wang, T., Jianrong, B., Shi, J., 2022. Polarization lidar measurements of dust optical properties at the junction of the Taklimakan Desert–Tibetan plateau. *Rem. Sens.* 14, 558. <https://doi.org/10.3390/rs14030558>.
- Dubovik, O., Smirnov, A., Holben, B., King, M., Kaufman, Y.J., Eck, T., Slutsker, I., 2000. Accuracy assessment of aerosol optical properties retrieved from Aerosol Robotic Network (AERONET) Sun and sky radiance measurements. *J. Geophys. Res.* Atmos. 105, 9791–9806. <https://doi.org/10.1029/2000JD900040>.
- Eck, T., Holben, B., Reid, J., Dubovik, O., Smirnov, A., Neill, Slutsker, I., Kinne, S., 1999. Wavelength dependence of the optical depth of biomass burning, urban, and desert dust aerosols. *J. Geophys. Res.* Atmos. 104, 31333–31349. <https://doi.org/10.1029/1999JD900923>.
- Fernald, F., 1984. Analysis of atmospheric lidar observations: some comments. *Appl. Opt.* 23, 652–653. <https://doi.org/10.1364/AO.23.000652>.
- Filonchik, M., Peterson, M., Hurynovich, V., 2021. Air pollution in the Gobi Desert region: analysis of dust-storm events. *Q. J. R. Meteorol. Soc.* 147, 1097–1111. <https://doi.org/10.1002/qj.3961>.
- Filonchik, M., Peterson, M.P., Zhang, L., Yan, H., 2024. An analysis of air pollution associated with the 2023 sand and dust storms over China: aerosol properties and PM10 variability. *Geosci. Front.* 15, 101762. <https://doi.org/10.1016/j.gsf.2023.101762>.
- Fu, Q., Liou, K.N., 1992. On the correlated k-distribution method for radiative transfer in nonhomogeneous atmospheres. *J. Atmos. Sci.* 49, 2139–2156. [https://doi.org/10.1175/1520-0469\(1992\)049<2139:OTCDMF>2.0.CO;2](https://doi.org/10.1175/1520-0469(1992)049<2139:OTCDMF>2.0.CO;2).
- Fu, Q., Liou, K.N., 1993. Parameterization of the radiative properties of cirrus clouds. *J. Atmos. Sci.* 50, 2008–2025. [https://doi.org/10.1175/1520-0469\(1993\)050<2008:POTRPO>2.0.CO;2](https://doi.org/10.1175/1520-0469(1993)050<2008:POTRPO>2.0.CO;2).
- Ge, J., Huang, J., Su, J., Jianrong, B., Fu, Q., 2011. Shortwave radiative closure experiment and direct forcing of dust aerosol over northwestern China. *Geophys. Res. Lett.* 38, 24803. <https://doi.org/10.1029/2011GL049571>.
- Ge, J., Su, J., Ackerman, T., Fu, Q., Huang, J., Shi, J., 2010. Dust aerosol optical properties retrieval and radiative forcing over northwestern China during the 2008 China-U.S. joint field experiment. *J. Geophys. Res.* Atmos. 115, D00K12. <https://doi.org/10.1029/2009JD013263>.
- Gelaro, R., McCarty, W., Suárez, M.J., Todling, R., Molod, A., Takacs, L., Randles, C.A., Darmenov, A., Bosilovich, M.G., Reichle, R., Wang, K., Coy, L., Cullather, R., Draper, C., Akella, S., Buchard, V., Conaty, A., da Silva, A.M., Gu, W., Kim, G.-K., Koster, R., Lucchesi, R., Merkova, D., Nielsen, J.E., Parityka, G., Pawson, S., Putman, W., Rienecker, M., Schubert, S.D., Sienkiewicz, M., Zhao, B., 2017. The modern-Era Retrospective analysis for research and Applications, version 2 (MERRA-2). *J. Clim.* 30, 5419–5454. <https://doi.org/10.1175/JCLI-D-16-0758.1>.
- Giles, D.M., Sinyuk, A., Sorokin, M.G., Schafer, J.S., Smirnov, A., Slutsker, I., Eck, T.F., Holben, B.N., Lewis, J.R., Campbell, J.R., Welton, E.J., Korkin, S.V., Lyapustin, A.I., 2019. Advancements in the Aerosol Robotic Network (AERONET) Version 3 database – automated near-real-time quality control algorithm with improved cloud screening for Sun photometer aerosol optical depth (AOD) measurements. *Atmos. Meas. Tech.* 12, 169–209. <https://doi.org/10.5194/amt-12-169-2019>.
- Gillette, D.A., Bodhaine, B.A., Mackinnon, D., 1993. Transport and deposition of desert dust in the kafirnigan river valley (Tadzhikistan) from Shaartuz to esanbay: measurements and a simple model. *Atmospheric environment. Part A. General Topics* 27, 2545–2552. [https://doi.org/10.1016/0960-1686\(93\)90028-W](https://doi.org/10.1016/0960-1686(93)90028-W).
- Golitsyn, G., Gillette, D.A., 1993. Introduction: a joint Soviet-American experiment for the study of Asian desert dust and its impact on local meteorological conditions and climate. *Atmospheric Environment. Part A. General Topics.* 27, 2467–2470. [https://doi.org/10.1016/0960-1686\(93\)90017-S](https://doi.org/10.1016/0960-1686(93)90017-S).
- Hersbach, H., Bell, B., Berrisford, P., Hirahara, S., Horányi, A., Muñoz-Sabater, J., Nicolas, J., Peubey, C., Radu, R., Schepers, D., Simmons, A., Soci, C., Abdalla, S., Abellan, X., Balsamo, G., Bechtold, P., Biavati, G., Bidlot, J., Bonavita, M., De Chiara, G., Dahlgren, P., Dee, D., Diamantakis, M., Dragani, R., Flemming, J., Forbes, R., Fuentes, M., Geer, A., Haimberger, L., Healy, S., Hogan, R.J., Hólm, E., Janisková, M., Keeley, S., Laloyaux, P., Lopez, P., Lupu, C., Radnoti, G., de Rosnay, P., Rozum, I., Vamborg, F., Villaume, S., Thépaut, J.-N., 2020. The ERA5 global reanalysis. *Q. J. R. Meteorol. Soc.* 146, 1999–2049. <https://doi.org/10.1002/qj.3803>.
- Hofer, J., Althausen, D., Abdullaev, S.F., Makhmudov, A.N., Nazarov, B.I., Schettler, G., Engelmann, R., Baars, H., Fomba, K.W., Müller, K., Heinzold, B., Kandler, K., Ansmann, A., 2017. Long-term profiling of mineral dust and pollution aerosol with multiwavelength polarization Raman lidar at the Central Asian site of Dushanbe, Tajikistan: case studies. *Atmos. Chem. Phys.* 17, 14559–14577. <https://doi.org/10.5194/acp-17-14559-2017>.
- Hofer, J., Ansmann, A., Althausen, D., Engelmann, R., Baars, H., Abdullaev, S.F., Makhmudov, A.N., 2020. Long-term profiling of aerosol light extinction, particle mass, cloud condensation nuclei, and ice-nucleating particle concentration over Dushanbe, Tajikistan, in Central Asia. *Atmos. Chem. Phys.* 20, 4695–4711. <https://doi.org/10.5194/acp-20-4695-2020>.
- Holben, B., Eck, T., Slutsker, I., Smirnov, A., Sinyuk, A., Schafer, J., Giles, D., Dubovik, O., 2006. AERONET's version 2.0 quality assurance criteria. *Remote Sensing of Atmosphere and Clouds* 6408, 134–147. <https://doi.org/10.1117/12.706524>.
- Holben, B.N., Eck, T.F., Slutsker, I., Tanré, D., Buis, J.P., Setzer, A., Vermote, E., Reagan, J.A., Kaufman, Y.J., Nakajima, T., Lavenu, F., Jankowiak, I., Smirnov, A., 1998. AERONET—a federated instrument network and data archive for aerosol characterization. *Remote Sensing of Environment* 66, 1–16. [https://doi.org/10.1016/S0034-4257\(98\)00031-5](https://doi.org/10.1016/S0034-4257(98)00031-5).
- Hu, Q., Han, Z., 2022. Northward expansion of desert climate in central Asia in recent decades. *Geophys. Res. Lett.* 49, e2022GL098895. <https://doi.org/10.1029/2022GL098895>.
- Hua, L., Zhao, T., Zhong, L., 2022. Future changes in drought over Central Asia under CMIP6 forcing scenarios. *J. Hydrol.: Reg. Stud.* 43, 101191. <https://doi.org/10.1016/j.ejrh.2022.101191>.
- Huang, J., Fu, Q., Su, J., Tang, Q., Minnis, P., Hu, Y., Yi, Y., Zhao, Q., 2009. Taklimakan dust aerosol radiative heating derived from CALIPSO observations using the Fu-Liou radiation model with CERES constraints. *Atmos. Chem. Phys.* 9, 4011–4021. <https://doi.org/10.5194/acp-9-4011-2009>.
- Huang, J., Wang, T., Wang, W., Li, Z., Yan, H., 2014. Climate effects of dust aerosols over East Asian arid and semiarid regions. *J. Geophys. Res.* Atmos. 119, 31146–31146. <https://doi.org/10.1002/2014JD021796>.
- Huang, Z., Dong, Q., Chen, B., Wang, T., Jianrong, B., Zhou, T., Alam, K., Shi, J., Zhang, S., 2023. Method for retrieving range-resolved aerosol microphysical properties from polarization lidar measurements. *Opt Express* 31, 7599–7616. <https://doi.org/10.1364/OE.481252>.
- Huang, Z., Huang, J., Bi, J., Wang, G., Wang, W., Fu, Q., Li, Z., Tsay, S.-C., Shi, J., 2010. Dust aerosol vertical structure measurements using three MPL lidars during 2008 China-U.S. joint dust field experiment. *J. Geophys. Res.* Atmos. 115, D00K15. <https://doi.org/10.1029/2009JD013273>.
- Huang, Z., Nee, J., Chiang, C.-W., Zhang, S., Jin, H., Wencai, W., Zhou, T., 2018. Real-time observations of dust–cloud interactions based on polarization and Raman lidar measurements. *Rem. Sens.* 10, 1017. <https://doi.org/10.3390/rs10071017>.
- Huang, Z., Siqu, Q., Zhou, T., Dong, Q., Ma, X., Zhang, S., Jianrong, B., Shi, J., 2020. Investigation of aerosol absorption with dual-polarization lidar observations. *Opt Express* 28, 7028–7035. <https://doi.org/10.1364/OE.390475>.
- Intergovernmental Panel on Climate Change, 2023. *Climate Change 2023 – The Physical Science Basis: Working Group I Contribution to the Sixth Assessment Report of the Intergovernmental Panel on Climate Change*. Cambridge University Press, Cambridge. <https://doi.org/10.1017/9781009157896>.
- Jordan, A.K., Gnanadesikan, A., Zaitchik, B., 2018. Simulated dust aerosol impacts on western sahelian rainfall: importance of ocean coupling. *J. Clim.* 31, 9107–9124. <https://doi.org/10.1175/JCLI-D-17-0819.1>.
- Justice, C.O., Townshend, J.R.G., Vermote, E.F., Masuoka, E., Wolfe, R.E., Saleous, N., Roy, D.P., Morisette, J.T., 2002. An overview of MODIS Land data processing and product status. *Remote Sensing of Environment* 83, 3–15. [https://doi.org/10.1016/S0034-4257\(02\)00084-6](https://doi.org/10.1016/S0034-4257(02)00084-6).
- Kanniah, K.D., Kamarul Zaman, N.A.F., Kaskaoutis, D.G., Latif, M.T., 2020. COVID-19's impact on the atmospheric environment in the Southeast Asia region. *Sci. Total Environ.* 736, 139658. <https://doi.org/10.1016/j.scitotenv.2020.139658>.
- Kaskaoutis, D., Singh, R., Gautam, R., Sharma, M., Kosmopoulos, P., Tripathi, S., 2012. Variability and trends of aerosol properties over Kanpur, northern India using AERONET data (2001–10). *Environ. Res. Lett.* 7, 24003–24009. <https://doi.org/10.1088/1748-9326/7/2/024003>.

- Klüser, L., Schepanski, K., 2009. Remote sensing of mineral dust over land with MSG infrared channels: a new Bitemporal Mineral Dust Index. *Remote Sensing of Environment* 113, 1853–1867. <https://doi.org/10.1016/j.rse.2009.04.012>.
- Kok, J., Storelvmo, T., Karydis, V., Adebisi, A., Mahowald, N., Evan, A., He, C., Leung, D., 2023. Mineral dust aerosol impacts on global climate and climate change. *Nat. Rev. Earth Environ.* 4, 71–86. <https://doi.org/10.1038/s43017-022-00379-5>.
- Kok, J.F., Ridley, D.A., Zhou, Q., Miller, R.L., Zhao, C., Heald, C.L., Ward, D.S., Albani, S., Haustein, K., 2017. Smaller desert dust cooling effect estimated from analysis of dust size and abundance. *Nat. Geosci.* 10, 274–278. <https://doi.org/10.1038/ngeo2912>.
- Kokkalis, P., Soupiona, O., Papanikolaou, C.-A., Foskinis, R., Mylonaki, M., Solomos, S., Vratolis, S., Vasilatou, V., Kralli, E., Anagnou, D., Papayannis, A., 2021. Radiative effect and mixing Processes of a long-lasting dust event over Athens, Greece, during the COVID-19 period. *Atmosphere* 12, 318. <https://doi.org/10.3390/atmos12030318>.
- Levelt, P.F., Joiner, J., Tamminen, J., Veefkind, J.P., Bhartia, P.K., Stein Zweers, D.C., Duncan, B.N., Streets, D.G., Eskes, H., van der A, R., McLinden, C., Fioletov, V., Carn, S., de Laat, J., DeLand, M., Marchenko, S., McPeters, R., Ziemke, J., Fu, D., Liu, X., Pickering, K., Apituley, A., González Abad, G., Arola, A., Boersma, F., Chan Miller, C., Chance, K., de Graaf, M., Hakkarainen, J., Hassinen, S., Ialongo, I., Kleipool, Q., Krotkov, N., Li, C., Lamsal, L., Newman, P., Nowlan, C., Suleiman, R., Tilstra, L.G., Torres, O., Wang, H., Wargan, K., 2018. The ozone monitoring instrument: overview of 14 years in space. *Atmos. Chem. Phys.* 18, 5699–5745. <https://doi.org/10.5194/acp-18-5699-2018>.
- Li, F., Vogelmann, A.M., Ramanathan, V., 2004. Saharan dust aerosol radiative forcing measured from space. *J. Clim.* 17, 2558–2571. [https://doi.org/10.1175/1520-0442\(2004\)017<2558:SDARFM>2.0.CO;2](https://doi.org/10.1175/1520-0442(2004)017<2558:SDARFM>2.0.CO;2).
- Li, L., Sokolik, I.N., 2018. The dust direct radiative impact and its sensitivity to the land surface state and key minerals in the WRF-chem-DuMo model: a case study of dust storms in central Asia. *J. Geophys. Res. Atmos.* 123, 4564–4582. <https://doi.org/10.1029/2017JD027667>.
- Li, Z., Bi, J., Hu, Z., Ma, J., Li, B., 2023. Regional transportation and influence of atmospheric aerosols triggered by Tonga volcanic eruption. *Environmental Pollution* 325, 121429. <https://doi.org/10.1016/j.envpol.2023.121429>.
- Liao, H., Seinfeld, J., 1998. Radiative forcing by mineral dust aerosols: sensitivity to key variables. *J. Geophys. Res. Atmos.* 103, 31637–31646. <https://doi.org/10.1029/1998JD200036>.
- Lioubimtseva, E., Henebry, G.M., 2009. Climate and environmental change in arid Central Asia: impacts, vulnerability, and adaptations. *J. Arid Environ.* 73, 963–977. <https://doi.org/10.1016/j.jaridenv.2009.04.022>.
- Liu, Q., Huang, Z., Liu, J., Chen, W., Dong, Q., Wu, S., Dai, G., Li, M., Li, W., Li, Z., Song, X., Xie, Y., 2024. Validation of initial observation from the first spaceborne high-spectral-resolution lidar with a ground-based lidar network. *Atmos. Meas. Tech.* 17, 1403–1417. <https://doi.org/10.5194/amt-17-1403-2024>.
- Liu, X., Chen, S., Guo, Z., Zhou, H., Chen, Y., Kang, Y., Liu, Q., Huang, G., Liu, T., Chen, C., He, Q., 2021. The influence of dusts on radiation and temperature over the eastern Asia with a regional climate model. *Sci. Total Environ.* 792, 148351. <https://doi.org/10.1016/j.scitotenv.2021.148351>.
- Liu, Z., Sugimoto, N., Murayama, T., 2002. Extinction-to-backscatter ratio of Asian dust observed with high-spectral-resolution lidar and Raman lidar. *Appl. Opt.* 41, 2760–2767. <https://doi.org/10.1364/AO.41.002760>.
- Meloni, D., Junkermann, W., di Sarra, A., Cacciani, M., De Silvestri, L., Di Iorio, T., Estellés, V., Gómez-Amo, J.L., Pace, G., Sferlatto, D.M., 2015. Altitude-resolved shortwave and longwave radiative effects of desert dust in the Mediterranean during the GAMARF campaign: indications of a net daily cooling in the dust layer. *J. Geophys. Res. Atmos.* 120, 3386–3407. <https://doi.org/10.1002/2014JD022312>.
- Miller, R.L., Perlwitz, J., Tegen, I., 2004. Modeling Arabian dust mobilization during the Asian summer monsoon: the effect of prescribed versus calculated SST. *Geophys. Res. Lett.* 31, L22214. <https://doi.org/10.1029/2004GL020669>.
- Pan, B., Wang, Y., Lin, Y., Hsieh, J.-S., Lavallee, M., Zhao, L., Zhang, R., 2024. Radiative and microphysical impacts of the saharan dust on two concurrent tropical cyclones: danielle and earl (2010). *J. Geophys. Res. Atmos.* 129, e2023JD039245. <https://doi.org/10.1029/2023JD039245>.
- Pandithurai, G., Dipu, S., Dani, K., Tiwari, S., Bisht, D., Devara, P., Pinker, R., 2008. Aerosol radiative forcing during dust events over New Delhi, India. *J. Geophys. Res. Atmos.* 113, D13209. <https://doi.org/10.1029/2008JD009804>.
- Peris, C., Gómez-Amo, J., Marcos-Segovia, C., Freile-Aranda, M., Utrillas, M., Martínez-Lozano, J., 2017. Heating rate profiles and radiative forcing due to a dust storm in the Western Mediterranean using satellite observations. *Atmos. Environ.* 160, 142–153. <https://doi.org/10.1016/j.atmosenv.2017.04.023>.
- Quijano, A.L., Sokolik, I.N., Toon, O.B., 2000. Radiative heating rates and direct radiative forcing by mineral dust in cloudy atmospheric conditions. *J. Geophys. Res. Atmos.* 105, 12207–12219. <https://doi.org/10.1029/2000JD900047>.
- Ricchiazzi, P., Yang, S., Gautier, C., Sowle, D., 1998. SBDART: a research and teaching software tool for plane-parallel radiative transfer in the Earth's atmosphere. *Bull. Am. Meteorol. Soc.* 79, 2101–2114. [https://doi.org/10.1175/1520-0477\(1998\)079<2101:SARATS>2.0.CO;2](https://doi.org/10.1175/1520-0477(1998)079<2101:SARATS>2.0.CO;2).
- Rupakheti, D., Rupakheti, M., Abdullaev, S.F., Yin, X., Kang, S., 2020. Columnar aerosol properties and radiative effects over Dushanbe, Tajikistan in Central Asia. *Environmental Pollution* 265, 114872. <https://doi.org/10.1016/j.envpol.2020.114872>.
- Rupakheti, D., Rupakheti, M., Yin, X., Hofer, J., Rai, M., Hu, Y., Abdullaev, S.F., Kang, S., 2021. Modifications in aerosol physical, optical and radiative properties during heavy aerosol events over Dushanbe, Central Asia. *Geosci. Front.* 12, 101251. <https://doi.org/10.1016/j.gsf.2021.101251>.
- Ryder, C.L., Highwood, E.J., Walser, A., Seibert, P., Philipp, A., Weinzierl, B., 2019. Coarse and giant particles are ubiquitous in Saharan dust export regions and are radiatively significant over the Sahara. *Atmos. Chem. Phys.* 19, 15353–15376. <https://doi.org/10.5194/acp-19-15353-2019>.
- Saidou Chaibou, A.A., Ma, X., Sha, T., 2020. Dust radiative forcing and its impact on surface energy budget over West Africa. *Sci. Rep.* 10, 12236. <https://doi.org/10.1038/s41598-020-69223-4>.
- Sharma, D., Singh, D., Kaskaoutis, D., 2012. Impact of two intense dust storms on aerosol characteristics and radiative forcing over Patiala, northwestern India. *Adv. Meteorol.* 2012, 956814. <https://doi.org/10.1155/2012/956814>.
- Sicard, M., Bertolin, S., Mallet, M., Dubuisson, P., Comerón, A., 2014. Estimation of mineral dust long-wave radiative forcing: sensitivity study to particle properties and application to real cases in the region of Barcelona. *Atmos. Chem. Phys.* 14, 9213–9231. <https://doi.org/10.5194/acp-14-9213-2014>.
- Siqi, Q., Huang, Z., Ma, X., Huang, J., Zhou, T., Zhang, S., Dong, Q., Jianrong, B., Shi, J., 2021. Classification of atmospheric aerosols and clouds by use of dual-polarization lidar measurements. *Opt Express* 29, 23461–23476. <https://doi.org/10.1364/OE.430456>.
- Smirnov, V.V., Johnson, T.C., Krapivtseva, G.M., Krivchikova, T.V., Shukurov, A.H., 1993. Synoptic meteorological conditions during the U.S.S.R./U.S. dust experiment in Tadzhikistan in September 1989. *Atmospheric Environment. Part A. General Topics* 27, 2471–2479. [https://doi.org/10.1016/0960-1686\(93\)90018-T](https://doi.org/10.1016/0960-1686(93)90018-T).
- Sokolik, I., Golitsyn, G., 1993. Investigation of optical and radiative properties of atmospheric dust aerosols. *Atmospheric Environment. Part A. General Topics* 27, 2509–2517. [https://doi.org/10.1016/0960-1686\(93\)90023-R](https://doi.org/10.1016/0960-1686(93)90023-R).
- Sokolik, I., Toon, O., 1999. Incorporation of mineralogical composition into models of the radiative properties of mineral aerosol from UV to IR wavelengths. *J. Geophys. Res. Atmos.* 104, 9423–9444. <https://doi.org/10.1029/1998JD200048>.
- Soupiona, O., Papayannis, A., Kokkalis, P., Foskinis, R., Sánchez Hernández, G., Ortiz-Amezcua, P., Mylonaki, M., Papanikolaou, C.A., Papagiannopoulos, N., Samaras, S., Groß, S., Mamouri, R.E., Alados-Arboledas, L., Amodeo, A., Psiloglou, B., 2020. EARLINET observations of Saharan dust intrusions over the northern Mediterranean region (2014–2017): properties and impact on radiative forcing. *Atmos. Chem. Phys.* 20, 15147–15166. <https://doi.org/10.5194/acp-20-15147-2020>.
- Steinfeld, J.I., 1998. Atmospheric chemistry and physics: from air pollution to climate change. *Environment* 40, 26. <https://doi.org/10.1080/00139157.1999.10544295>.
- Su, L., Toon, O.B., 2011. Saharan and Asian dust: similarities and differences determined by CALIPSO, AERONET, and a coupled climate-aerosol microphysical model. *Atmos. Chem. Phys.* 11, 3263–3280. <https://doi.org/10.5194/acpd-10-29513-2010>.
- Valenzuela, A., Costa, M.J., Guerrero-Rascado, J.L., Bortoli, D., Olmo, F.J., 2017. Solar and thermal radiative effects during the 2011 extreme desert dust episode over Portugal. *Atmos. Environ.* 148, 16–29. <https://doi.org/10.1016/j.atmosenv.2016.10.037>.
- Victor, J., Potdar, S., Tamilselvam, G., Kamra, A., Singh, R.P., V G, V.G., Pandithurai, G., 2024. Impact of a severe dust storm on aerosol properties and their radiative forcing over the Indian subcontinent during winter. *Atmos. Res.* 301, 107282. <https://doi.org/10.1016/j.atmosres.2024.107282>.
- Wang, A., Xie, X., Liu, X., Yin, Z.-Y., 2022. Direct radiative effect (DRE) of dust aerosols on West African and East Asian monsoon: the role of ocean-atmosphere interactions. *J. Geophys. Res. Atmos.* 127, e2021JD035917. <https://doi.org/10.1029/2021JD035917>.
- Wang, T., Ying, H., Huang, J., Sun, M., Jian, B., Huang, Z., Yan, H., 2020. Climatology of dust-forced radiative heating over the Tibetan plateau and its surroundings. *J. Geophys. Res. Atmos.* 125, e2020JD032942. <https://doi.org/10.1029/2020JD032942>.
- Wang, W., Gong, W., Mao, F., Pan, Z., 2018. Physical constraint method to determine optimal overlap factor of Raman lidar. *J. Opt.* 47, 83–90. <https://doi.org/10.1007/s12596-017-0427-9>.
- Wang, X., Li, Y., Chen, Y., Li, Y., Wang, C., Kaldybayev, A., Gou, R., Luo, M., Duan, W., 2023. Intensification of heatwaves in Central Asia from 1981 to 2020 – role of soil moisture reduction. *J. Hydrol.* 627, 130395. <https://doi.org/10.1016/j.jhydrol.2023.130395>.
- Xie, X., Liu, X., Che, H., Xie, X., Wang, H., Li, J., Shi, Z., Liu, Y., 2018. Modeling East Asian dust and its radiative feedbacks in CAM4-BAM. *J. Geophys. Res. Atmos.* 123, 1079–1096. <https://doi.org/10.1002/2017JD027343>.
- Yalkun, A., Liu, S., Yang, F., He, Q., Qi, F., Liu, Y., 2019. Coefficients optimization of the GLASS broadband emissivity based on FTIR and MODIS data over the Taklimakan Desert. *Sci. Rep.* 9, 18460. <https://doi.org/10.1038/s41598-019-54982-6>.
- Yu, S., Yan, Z., Freychet, N., Li, Z., 2020. Trends in summer heatwaves in central Asia from 1917 to 2016: association with large-scale atmospheric circulation patterns. *Int. J. Climatol.* 40, 115–127. <https://doi.org/10.1002/joc.6197>.
- Zhang, D.F., Zakey, A.S., Gao, X.J., Giorgi, F., Solmon, F., 2009. Simulation of dust aerosol and its regional feedbacks over East Asia using a regional climate model. *Atmos. Chem. Phys.* 9, 1095–1110. <https://doi.org/10.5194/acp-9-1095-2009>.
- Zhang, S., Huang, Z., Alam, K., Li, M., Dong, Q., Wang, Y., Xingtai, S., Jianrong, B., Zhang, J., Li, W., Li, Z., Wang, W., Cui, Z., Song, X., 2023. Derived profiles of CCN and INP number concentrations in the Taklimakan Desert via combined polarization lidar, sun-photometer, and radiosonde observations. *Rem. Sens.* 15, 1216. <https://doi.org/10.3390/rs15051216>.
- Zhang, S., Huang, Z., Li, M., Xingtai, S., Wang, Y., Dong, Q., Jianrong, B., Zhang, J., Li, W., Li, Z., Song, X., 2022. Vertical structure of dust aerosols observed by a

- ground-based Raman lidar with polarization capabilities in the center of the Taklimakan Desert. *Rem. Sens.* 14, 2461. <https://doi.org/10.3390/rs14102461>.
- Zheng, Y., Guo, J., Ghent, D., Tansey, K., Hu, X., Nie, J., Chen, S., 2019. Land surface temperature retrieval from sentinel- 3A sea and land surface temperature radiometer, using a split-window algorithm. *Rem. Sens.* 11, 650. <https://doi.org/10.3390/rs11060650>.
- Zhu, D., Bi, J., Wang, X., Meng, Z., Shi, J., Li, O., 2024. Diurnal asymmetry of surface albedo in a semi-arid grassland over the China's Loess Plateau. *Atmos. Sci. Lett.* 25, e1271. <https://doi.org/10.1002/asl.1271>.